Resolving combinatorial ambiguities in dilepton $t\bar{t}$ event topologies with constrained M_2 variables

Dipsikha Debnath,[1] Doojin Kim,[2] Jeong Han Kim,[3] Kyoungchul Kong,[3,4] and Konstantin T. Matchev[1]

[1]*Physics Department, University of Florida, Gainesville, FL 32611, USA*
[2]*Theory Department, CERN, CH-1211 Geneva 23, Switzerland*
[3]*Department of Physics and Astronomy, University of Kansas, Lawrence, KS 66045, USA*
[4]*Pittsburgh Particle physics, Astrophysics, and Cosmology Center, Department of Physics and Astronomy, University of Pittsburgh, Pittsburgh, PA 15260, USA*

We advocate the use of on-shell constrained M_2 variables in order to mitigate the combinatorial problem in supersymmetry-like events with two invisible particles at the LHC. We show that in comparison to other approaches in the literature, the constrained M_2 variables provide superior ansätze for the unmeasured invisible momenta and therefore can be usefully applied to discriminate combinatorial ambiguities. We illustrate our procedure with the example of dilepton $t\bar{t}$ events. We critically review the existing methods based on the Cambridge M_{T2} variable and MAOS reconstruction of invisible momenta, and show that their algorithm can be simplified without loss of sensitivity, due to a perfect correlation between events with complex solutions for the invisible momenta and events exhibiting a kinematic endpoint violation. Then we demonstrate that the efficiency for selecting the correct partition is further improved by utilizing the M_2 variables instead. Finally, we also consider the general case when the underlying mass spectrum is unknown, and no kinematic endpoint information is available.

I. INTRODUCTION

Events with missing transverse energy[1] ($\rlap{/}{E}_T$) are arguably the most exciting class of events at the Large Hadron Collider (LHC). They offer the tantalizing possibility of discovering the elusive dark matter—if dark matter particles were produced in the LHC collisions, they would leave the detector without a trace, and the only sign of their presence would be the imbalance in the total transverse momentum of the event. Unfortunately, events with $\rlap{/}{E}_T$ are also notoriously difficult to interpret and analyze:

(a) *Instrumental effects.* Since the missing transverse momentum $\vec{\rlap{/}{P}}_T$ is measured only as the recoil against *all other* visible objects in the event, it can be easily faked by mismeasurement and the finite detector resolution [1]. This problem becomes more severe if the signature involves QCD jets, whose energies and momenta are poorly measured in comparison to leptons and photons.

(b) *Unknown nature of the invisible particles.* A priori, we do not know the nature of the invisible

particles—they could be new particles, or simply the Standard Model (SM) neutrinos [2].

(c) *Incomplete kinematic information.* We do not know how many invisible particles were present in the event to begin with [3–7]. We also do not know their individual momenta, and only the net sum $\vec{\rlap{/}{P}}_T$ of their transverse components is available.

The first step in the analysis of any sample of $\rlap{/}{E}_T$ events is to hypothesize a certain event topology, and design suitable variables adapted to this interpretation [8]. It is already at this stage that one is facing a combinatorial problem, namely, how to associate the various reconstructed objects in the event to the elementary particles in the final state of the event topology. Only in very special cases does the problem not arise—if the event topology is very simple and/or all final state particles are distinct. In general, a typical $\rlap{/}{E}_T$ event at the LHC does suffer from a combinatorics problem, for the following two reasons:

(a) At hadron colliders like the LHC, strong production of colored particles is the dominant production mechanism. When those colored particles decay to the invisible dark matter candidates, the color is shed in the form of QCD jets, which can be confused with jets from initial state radiation (ISR) [9–12]. In fact, the ISR combinatorics problem is very general and affects any multijet events at hadron colliders, regardless of the presence of $\rlap{/}{E}_T$ in the event.

(b) The lifetime of the dark matter particles is typically protected by some new symmetry. This is often chosen to be a discrete Z_2 parity, under which the

---

SM particles are even, while the new physics particles are odd. In that case, the new particles are necessarily pair produced, so that each event contains two independent decay chains. This creates a partitioning ambiguity, since the experimenter has to decide whether to assign each reconstructed object to the first or the second decay chain [13]. Wrong assignments would tend to wash out the desired kinematic features and degrade the measurements.

In principle, the combinatorial problem can be addressed in two different ways:

(a) *Sidestep the combinatorial problem.* The idea here is to design the analysis in such a way that the combinatorial problem does not become an issue. Two possibilities are:

   (i) *Use global inclusive variables which do not suffer from a combinatorics problem.* These variables treat the event as a whole and thus do not depend on the exact event topology, and the combinatorics problem does not arise in the first place. Some well known examples are $M_{\rm eff}$ [14,15], $\hat{s}_{\min}$ [16], $\not{E}_T$ [17], etc. The disadvantage is that such variables are suboptimal when compared to more exclusive variables which take advantage of the individual characteristics of the event topology.

   (ii) *Use variables which optimize over all possible combinatorial assignments.* In this case, instead of trying to figure out the correct assignment in a given event, one considers all possibilities, then chooses the one[2] which preserves the relevant useful property of the kinematic variable used in the analysis. As an example, consider an attempt to measure the *upper* kinematic endpoint of some relevant distribution, such as a two-body invariant mass or the Cambridge M_{T2} variable [18]. One could simply compute the value of the variable under all possible assignments, then choose the *smallest* among them to be used in the analysis [14,19–27].[3] While this procedure is guaranteed to preserve the kinematic endpoint, it also adversely distorts the shape of the kinematic distribution in the vicinity of the endpoint, making it more difficult to observe in the presence of SM background.

(b) *Resolve the combinatorial problem by choosing the "best" assignment event by event.* In this case one tries to design an algorithm which will single out one (or maybe several) among the many possible assignments as the most likely "correct" assignment, then use the value of the kinematic variable obtained with this specific choice. Ideally, the algorithm should return a unique selection, which would be correct 100% of the time. Unfortunately, this is rarely achievable in practice, and an important measure quantifying the success of the algorithm is the purity of the resulting sample, i.e., the fraction of events in which the combinatorics was successfully resolved. In principle, there can be different approaches to designing such an algorithm, from the use of a single exclusive variable to a multivariate technique like a neural network analysis [28]. For example, depending on the process at hand, one can attempt to tag ISR jets by a suitable combination of cuts on the jet rapidity and transverse momentum [29] or on the invariant mass and M_{T2} [30]. The partitioning problem into two decay chains is usually addressed by the so-called "hemisphere" algorithm, developed originally within CMS [31] and later adopted in many phenomenological studies [32–34]. There have been attempts to further improve on the hemisphere algorithm by suitable cuts on the invariant mass and either the jet p_T [35] or M_{T2} [36], by excluding certain reconstructed objects from the clustering algorithm [21,37], or by recursive jigsaw reconstruction [38]. In general, methods which invoke fewer assumptions, are robust and model independent, but lead to rather vague conclusions, while methods with more assumptions give better results, but are not generally applicable.

In the case of $\not{E}_T$ events, the combinatorics problem is exacerbated by the fact that the momenta of the invisible particles are unknown. If the decay chains are sufficiently long, so that there are enough kinematic constraints, one can attempt to compute the individual invisible particle momenta on an event per event basis [39–43]. Unfortunately, this procedure itself suffers from a combinatorics problem, which only becomes worse as the decay chains get longer (as required for the method to work). For shorter decay chains, like the ones considered in this paper, the method does not apply.

Since the invisible momenta cannot be reconstructed exactly, the next best thing to do is to use some sort of an approximation for them [44]. Again, different approaches are possible. For example, one could use a matrix element method (MEM) to select the most likely values of the invisible momenta. However, the MEM itself suffers from combinatorics, and is rather model dependent since it requires us to fully specify the underlying physics. A better approach would be to rely only on kinematics and obtain the invisible momenta by optimizing a suitable kinematic function. But what constitutes a good target function for such optimization? Initially, the focus was placed on *transverse* mass variables like M_{T2} [18,45] and

---

[2] The chosen option does not necessarily have to be the correct one.

[3] A similar idea can be applied to measure a *lower* kinematic endpoint—in that case one would choose the *largest* value among all possibilities.

its variants [46–49]. While transverse quantities are Lorentz invariant under longitudinal boosts, they only provide an ansatz for the *transverse* components of the individual invisible momenta, and one still needs to provide a supplementary procedure for calculating the *longitudinal* components of the invisible momenta. One such complementary technique is the MAOS[4] reconstruction [50], where one imposes an additional on-shell kinematic constraint which can be solved for the longitudinal momentum component of each invisible particle. It has been shown that the MAOS approach provides a reasonably good approximation to the true values of the invisible momenta, and can be usefully applied for mass and spin measurements [50–52]. The MAOS technique was then used to design a novel algorithm [53] for resolving the combinatorial ambiguity in dilepton $t\bar{t}$ events, further expanding on the ideas from Refs. [35,36]. The algorithm aims to resolve the two-fold[5] ambiguity in selecting the correct lepton-jet pairing and involves the following three steps:

Step I. Following the proposal of Ref. [36], some number of wrong lepton-jet combinations can be eliminated if they violate the expected endpoints in the distributions of the invariant mass $m_{b\ell}$ and M_{T2}.

Step II. Utilizing the ansatz found in Step I for the transverse components of the invisible momenta, attempt a MAOS reconstruction of the longitudinal components in two cases:

   1. using the known value of the top quark mass m_t;

   2. using the known value of the W-boson mass m_W.

Eliminate additional wrong combinations if the solutions for the longitudinal momenta in either case turn out to be complex.

Step III. In this final step, one uses the reconstructed masses for the W-boson (in case II.1) and the top quark (in case II.2) in conjunction with M_{T2} to decide which of the two lepton-jet pairings is the likelier one.

While this algorithm was originally designed to handle the two-fold ambiguity in $t\bar{t}$ events, where the mass spectrum is known, with suitable modifications it can also be applied to new physics searches, as advertised in Ref. [53]. For instance, in the MAOS reconstruction Step II, instead of using the fixed values of the known masses m_t and m_W, one could use the measured endpoints in the respective M_{T2} subsystems [46].

Recently it has been pointed out that the M_{T2} approach has a $(3 + 1)$-dimensional analogue in terms of a general class of on-shell constrained invariant mass variables M_2 [8,54,55]. Compared to M_{T2}, the M_2 variables have several advantages:

(a) Being defined in $(3 + 1)$ dimensions, they allow us to easily and directly enforce all relevant on-shell constraints in a given event topology [8,56].

(b) Unlike the case of M_{T2}, the optimization procedure required to compute the value of M_2 automatically provides an ansatz for both the transverse *and* the longitudinal components of the invisible momenta. In this sense, once one commits to using M_2 variables instead of M_{T2}, the MAOS reconstruction step for finding the longitudinal momentum components is unnecessary.

(c) The maximally constrained M_2 variable can be expected to provide the best possible ansatz for the individual invisible momenta, since it takes into account all relevant kinematic constraints in a given event topology [44].

The main goal of this paper is to utilize these advantages of the M_2 variables and design an improved algorithm for resolving the combinatorial ambiguity in supersymmetry-like events with two invisible particles at the LHC. As our benchmark, we shall use the current state of the art algorithm which was proposed and tested for dilepton $t\bar{t}$ events in Ref. [53]. Correspondingly, in Sec. II we shall first give a brief review of the relevant background information regarding the kinematics of the dilepton $t\bar{t}$ event topology. Then in Sec. III we shall carefully define the different options for kinematic reconstruction of the invisible momenta [44]. We shall see that in principle there can be different ways of applying the ideas of MAOS reconstruction, M_2-assisted reconstruction, or some combination of both. In Sec. III we shall also compare the accuracy of several representative methods for invisible momentum reconstruction.

The next three sections will be devoted to the issue of resolving the combinatorial ambiguity. First in Sec. IV we critically review each of the three steps of the current state of the art method based on the Cambridge M_{T2} variable and MAOS-reconstruction of invisible momenta [36,53]. Our goal will be to improve the algorithm in two aspects:

(a) *Better performance.* By considering various modifications, e.g., utilizing the alternative set of M_2 variables, or alternative implementations of the MAOS method itself, we shall attempt to improve the efficiency[6] of the algorithm in selecting the correct partition in dilepton $t\bar{t}$ events.

(b) *Simplicity.* At the same time, we shall keep an eye on the relative performance of each algorithm component, and if we find components which underperform, we shall eliminate them from consideration, thus simplifying the algorithm. For example, in

---

[4]MAOS stands for M_{T2}-Assisted On-Shell reconstruction.

[5]In the case of dilepton $t\bar{t}$ events, the two jets originating from the top decays can be distinguished from ISR jets by b-tagging.

[6]Throughout the paper, we shall use the terms "efficiency" and "purity" interchangeably to denote the same quantity—the fraction of events in which the algorithm is successful in identifying the correct partition.

Sec. IV B we shall demonstrate that Step II can be safely disregarded since it is fully correlated with Step I and does not give anything new.

Then in Sec. V we consider several new ideas which go beyond the three steps of the current algorithm. In Sec. V A we consider expanding the set of variables used in Step I from two to three, since the dilepton $t\bar{t}$ event topology allows not just two, but three independent kinematic endpoints [46,57]. Then in Sec. V B we discuss a special class of maximally constrained M_2 variables where the knowledge of the top and W-boson masses can be taken into account already during the optimization stage,[7] thus further improving the ansatz for the transverse invisible momenta. In Sec. V C we study the potential benefit from using a global inclusive variable such as $\sqrt{\hat{s}}$ or an angular variable such as the scattering angle of the parents in the center-of-mass frame. Finally, in Sec. VI we treat the general case when the underlying mass spectrum is unknown, and no kinematic endpoint information is available. We consider a simplified version of the algorithm which is suitably adapted to this scenario, and investigate its performance in the general new physics mass parameter space. We discuss future extensions of this work and summarize in Sec. VII.

II. DILEPTON $t\bar{t}$ KINEMATICS AND MASS-CONSTRAINING VARIABLES

In this section we shall introduce the basic notation and review the relevant class of mass-constraining variables which will be used later to obtain suitable ansätze for the invisible momenta. For the most part, we shall stick to the notation and terminology of Refs. [44,55]. Following [36,53], we focus primarily on the "dilepton $t\bar{t}$" event topology depicted in Fig. 1. This choice is motivated by several factors:

(a) As far as the combinatorial problem is concerned, this is the simplest example which is not trivial—if we were to consider a single-step two-body decay on each side, there would be no combinatorial issue to begin with, and if we were to consider longer decay chains, the problem would become more difficult.

(b) This event topology is realized in the SM production of $t\bar{t}$ events, providing a useful toy playground for testing new ideas for studying new physics [57–60].

(c) Several new physics models can lead to this event topology, including stop-pair production in supersymmetry [61] and pair-production of leptoquarkinos [62].

Thus the general event topology considered in this paper is the pair-production of two identical parent particles A_i, followed by a 2-step 2-body decay for each one (see Fig. 1):

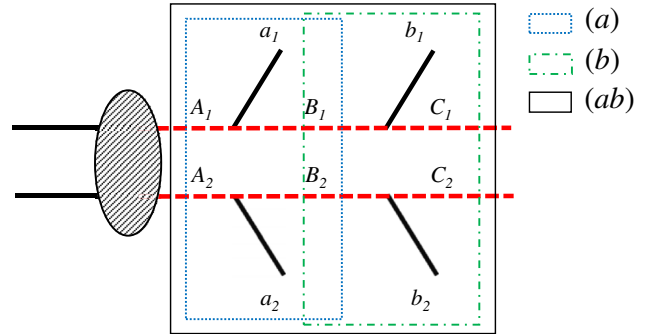[7]Note that this is impossible in the case of purely transverse variables like M_{T2}.

FIG. 1. The event topology considered in this paper, together with the three possible subsystems. The blue dotted, the green dot-dashed, and the black solid boxes indicate the subsystems (a), (b), and (ab), respectively. The figure is taken from Ref. [55].

$$pp \to A_1 A_2, \quad A_i \to a_i B_i, \quad B_i \to b_i C_i, \quad (i = 1, 2). \quad (1)$$

In principle, A_i, B_i and C_i should be thought of as some unknown beyond Standard Model (BSM) particles, while a_i and b_i are SM particles whose four-momenta are measured. The particles C_i are invisible in the detector, and their momenta q_i are constrained only by the $\vec{P}_T$ measurement and their (a priori unknown) masses, $\tilde{m}_{C_i}$, with $q_i^2 = \tilde{m}_{C_i}^2$.

The 2-step 2-body event topology of Fig. 1 allows for three different subsystems, as indicated by the colored rectangular boxes [46]. Each subsystem is labelled by the visible particles in it, and defined by a choice of parent and daughter particles, leaving the third type of particles as "relatives": in subsystem (ab) the parents are A_i, the daughters are C_i and the relatives are B_i; in subsystem (a) the parents are A_i, the daughters are B_i and the relatives are C_i, while in subsystem (b) the parents are B_i, the daughters are C_i and the relatives are A_i. The mass-constraining kinematic variables defined below can be applied to any of the three subsystems, thus each variable has three different versions, depending on the chosen subsystem. For simplicity, in what follows we shall assume that the event topology of Fig. 1 is symmetric, i.e., $A_1 = A_2$, $B_1 = B_2$, and $C_1 = C_2$ (see [47,48] for generalizing to the asymmetric case).

We first consider the traditional transverse variable M_{T2} [18]. Let the two transverse masses of the parent particles be $M_{TP_i}(\vec{q}_{iT}, \tilde{m})$, where $\vec{q}_{iT}$ is the transverse momentum of C_i and $\tilde{m}$ is a test mass for the daughter particles, which is $\tilde{m}_{C_i}$ for the case of subsystems (ab) and (b) and $\tilde{m}_{B_i}$ for the case of subsystem (a). The kinematic variable M_{T2} is now defined as the absolute minimum of the larger of these two transverse masses, with respect to all possible partitions of the individual invisible transverse momenta $\vec{q}_{iT}$,

$$M_{T2}(\tilde{m}) \equiv \min_{\vec{q}_{1T}, \vec{q}_{2T}} \{ \max [M_{TP_1}(\vec{q}_{1T}, \tilde{m}), M_{TP_2}(\vec{q}_{2T}, \tilde{m})] \}.$$

$$\vec{q}_{1T} + \vec{q}_{2T} = \vec{P}_T \quad (2)$$

Alternatively, one could apply the same procedure to the *actual* parent masses, M_{P_i}, and define the $(3+1)$-dimensional analogue of Eq. (2) as

$$M_2(\tilde{m}) \equiv \min_{\vec{q}_1, \vec{q}_2} \{\max [M_{P_1}(\vec{q}_1, \tilde{m}), M_{P_2}(\vec{q}_2, \tilde{m})]\},$$
$$\vec{q}_{1T} + \vec{q}_{2T} = \vec{P}_T \qquad (3)$$

where now the minimization is performed over the 3-component momentum vectors $\vec{q}_1$ and $\vec{q}_2$ [8]. As shown in Refs. [8,55,56], at this point the two definitions (2) and (3) are equivalent, in the sense that the resulting two variables, M_{T2} and M_2, will have the same numerical value.

The case when M_2 begins to differ from M_{T2} is when we start to apply additional kinematic constraints beyond the $\vec{P}_T$ condition $\vec{q}_{1T} + \vec{q}_{2T} = \vec{P}_T$. Then the M_2 variable can be further refined and one can obtain non-trivial variations [55]:

$$M_{2XX} \equiv \min_{\vec{q}_1, \vec{q}_2} \{\max [M_{P_1}(\vec{q}_1, \tilde{m}), M_{P_2}(\vec{q}_2, \tilde{m})]\},$$
$$\vec{q}_{1T} + \vec{q}_{2T} = \vec{P}_T \qquad (4)$$

$$M_{2CX} \equiv \min_{\vec{q}_1, \vec{q}_2} \{\max [M_{P_1}(\vec{q}_1, \tilde{m}), M_{P_2}(\vec{q}_2, \tilde{m})]\},$$
$$\vec{q}_{1T} + \vec{q}_{2T} = \vec{P}_T$$
$$M_{P_1} = M_{P_2} \qquad (5)$$

$$M_{2XC} \equiv \min_{\vec{q}_1, \vec{q}_2} \{\max [M_{P_1}(\vec{q}_1, \tilde{m}), M_{P_2}(\vec{q}_2, \tilde{m})]\},$$
$$\vec{q}_{1T} + \vec{q}_{2T} = \vec{P}_T$$
$$M_{R_1}^2 = M_{R_2}^2 \qquad (6)$$

$$M_{2CC} \equiv \min_{\vec{q}_1, \vec{q}_2} \{\max [M_{P_1}(\vec{q}_1, \tilde{m}), M_{P_2}(\vec{q}_2, \tilde{m})]\}.$$
$$\vec{q}_{1T} + \vec{q}_{2T} = \vec{P}_T$$
$$M_{P_1} = M_{P_2}$$
$$M_{R_1}^2 = M_{R_2}^2 \qquad (7)$$

Here M_{P_i} (M_{R_i}) is the reconstructed mass of the parent (relative) particle in the i-th decay chain during the associated minimization procedure and a subscript "C" indicates that an equal mass constraint is applied for the two parents (when "C" is in the first position) or for the relatives (when "C" is in the second position). A subscript "X" simply means that no such constraint is applied. In any given subsystem, the variables (2)–(7) are related event-by-event in the following way [55]

$$M_{T2} = M_{2XX} = M_{2CX} \leq M_{2XC} \leq M_{2CC}. \qquad (8)$$

Until now, we have treated the event topology of Fig. 1 in very general terms. In particular, we have not made any assumptions about the nature of the visible particles a_i and b_i. If they are all indistinguishable, e.g., jets from gluino pair-production events, $pp \to \tilde{g}\tilde{g} \to jj\tilde{q}\tilde{q} \to jjjj + \not{E}_T$, the resulting combinatorial issues are rather severe, and one should perhaps first focus on testing the hypothesis for the event topology [22]. Here we would like to start with a more tractable problem, where some of the final state particles are distinguishable. Keeping in mind the dilepton $t\bar{t}$ example and the analogous BSM signatures, we shall take particles a_i to be b-jets, and particles b_i to be leptons, i.e., $a_1 = b$, $a_2 = \bar{b}$, $b_1 = \ell^+$ and $b_2 = \ell^-$, where $\ell = \{e, \mu\}$ and b is the bottom quark. Since the charge of the b-jet is difficult to determine, there is a two-fold partitioning ambiguity: the correct partition is

$$P_C: \{b, \ell^+\} \oplus \{\bar{b}, \ell^-\}, \qquad (9)$$

while the wrong partition is

$$P_W: \{\bar{b}, \ell^+\} \oplus \{b, \ell^-\}. \qquad (10)$$

In the rest of this paper, we shall be concerned with designing algorithms which would preferentially select the correct pairing (9) over the wrong one (10). For this purpose, we shall mostly utilize the Cambridge M_{T2} variable (2) and the constrained M_{2CC} variable (7). Each of these two variables can be applied to one of the three possible $t\bar{t}$ subsystems, $(b\ell)$, (ℓ) and (b). Notice, however, that in the "smaller" subsystems (b) and (ℓ), the two partitions (9) and (10) give identical values of M_{T2}, thus the corresponding subsystem M_{T2} variables $M_{T2}^{(b)}$ and $M_{T2}^{(\ell)}$ will not be useful to us for the purposes of resolving the combinatorial issue. In contrast, all three subsystem M_{2CC} variables, $M_{2CC}^{(b\ell)}$, $M_{2CC}^{(b)}$, and $M_{2CC}^{(\ell)}$, depend on the partitioning—either directly, or through the relative constraint $M_{R_1} = M_{R_2}$.

Recently, Ref. [44] introduced another interesting variation of the M_{2CC} variable, which takes advantage of the potentially known mass for a relative particle. For example, if the mass of the B_i particles is known, we can enforce it as an additional constraint during the minimization in the (ab) subsystem. Specifying to the $t\bar{t}$ case, where A_i are the top quarks t_i and B_i are the W-bosons W_i, we can write

$$M_{2CW}^{(b\ell)} \equiv \min_{\vec{q}_1, \vec{q}_2} \{\max [M_{t_1}(\vec{q}_1, \tilde{m}), M_{t_2}(\vec{q}_2, \tilde{m})]\},$$
$$\vec{q}_{1T} + \vec{q}_{2T} = \vec{P}_T$$
$$M_{t_1} = M_{t_2}$$
$$M_{W_1} = M_{W_2} = m_W \qquad (11)$$

TABLE I. Various methods for reconstructing the transverse and longitudinal momenta of invisible particles in the dilepton $t\bar{t}$ event topology of Fig. 1. In all cases, one must specify a test mass for the lightest particle (the neutrino), then superscripts $(b\ell)$ and (ℓ) are used to denote respectively the (ab) and (b) subsystems of Fig. 1 (or alternatively, the subsystems (2,2,0) and (2,1,0) in the notation of Ref. [46]). The methods in the yellow (orange) cells will be investigated in detail in Table IX (Table XI) below.

Schemes for fixing the components of the invisible momenta					
longitudinal	transverse				
input	$M_{T2}^{(b\ell)} = M_{2CX}^{(b\ell)}$	$M_{T2}^{(\ell)} = M_{2CX}^{(\ell)}$	$M_{2CC}^{(b\ell)}$	$M_{2CC}^{(\ell)}$
m_t	MAOS1($b\ell;m_t$)	MAOS4($\ell;m_t$)	CMAOS1($b\ell;m_t$)	CMAOS4($\ell;m_t$)
m_W	MAOS4($b\ell;m_W$)	MAOS1($\ell;m_W$)	CMAOS4($b\ell;m_W$)	CMAOS1($\ell;m_W$)
$M_{T2}^{(b\ell)}$	MAOS2($b\ell;b\ell$)	MAOS2($\ell;b\ell$)	CMAOS2($b\ell;b\ell$)	CMAOS2($\ell;b\ell$)
$M_{T2}^{(\ell)}$	MAOS2($b\ell;\ell$)	MAOS2($\ell;\ell$)	CMAOS2($b\ell;\ell$)	CMAOS2($\ell;\ell$)
$M_{T}^{(b\ell)}$	MAOS3($b\ell;b\ell$)	MAOS3($\ell;b\ell$)	CMAOS3($b\ell;b\ell$)	CMAOS3($\ell;b\ell$)
$M_{T}^{(\ell)}$	MAOS3($b\ell;\ell$)	MAOS3($\ell;\ell$)	CMAOS3($b\ell;\ell$)	CMAOS3($\ell;\ell$)
$M_{2CC}^{(b\ell)}$	—	—	M$_2$A($b\ell$)	—
$M_{2CC}^{(\ell)}$	—	—	—	M$_2$A(ℓ)

where m_W is the experimentally measured W-boson mass. Similarly, if we take the mass m_t of the top quarks to be known, there is a new variable in the (ℓ) subsystem:

$$M_{2Ct}^{(\ell)} \equiv \min_{\vec{q}_1,\vec{q}_2}\{\max[M_{W_1}(\vec{q}_1,\tilde{m}), M_{W_2}(\vec{q}_2,\tilde{m})]\}.$$

$$\vec{q}_{1T} + \vec{q}_{2T} = \vec{\not{P}}_T$$

$$M_{W_1} = M_{W_2}$$

$$M_{t_1} = M_{t_2} = m_t \qquad (12)$$

III. RECONSTRUCTION SCHEMES FOR INVISIBLE MOMENTA

All of the kinematic variables introduced in the previous section are defined in terms of an optimization procedure over all possible values of the individual invisible momenta. The procedure then singles out one particular choice of the invisible momenta, which is used to calculate the corresponding variable. We can also use this choice as a useful ansatz for the invisible momenta, and then apply standard analysis techniques as if the momenta of the invisible particles were known [44,50].

The two main goals of this section are:

(a) to list systematically the different ways in which the variables from the previous section can be used (sometimes in combination) to obtain an ansatz for the invisible momenta (see Table I);

(b) to compare the accuracy of several representative schemes for invisible momentum reconstruction (see Figs. 2–4).

The ansatz for the invisible momenta is generally obtained in two steps[8]:

1. *Fixing the transverse components $\vec{q}_{iT}$ of the invisible momenta.* In principle, there are several possible options here: one can use either an M_{T2} variable, or an M_2 variable, which can then be applied to any of the three possible subsystems in Fig. 1. In addition, if one wished to use the mass information for a relative particle, one could also consider the maximally constrained variables (11) and (12). The four columns of Table I list four representative examples, illustrating both the use of different variables (M_{T2} versus M_{2CC}) and the use of different subsystems [$(b\ell)$ versus (ℓ)].

2. *Fixing the longitudinal components q_{iz} of the invisible momenta.* Having thus determined the transverse invisible components, the second step is to obtain values for the longitudinal components q_{iz} of the invisible momenta. There are several possibilities (refer to Table I):

(a) *Classic MAOS with mass information (MAOS1 and MAOS4).* In the original MAOS approach [50], a mass shell constraint for an intermediate resonance is imposed on each side of the event. Following the notation of [44], we shall make the distinction between cases where the resonance is a parent particle (MAOS1) and a relative particle (MAOS4). In the classic MAOS

---

[8]In all cases, one must specify a test mass for the lightest particle (the neutrino in the case of dilepton $t\bar{t}$ events.
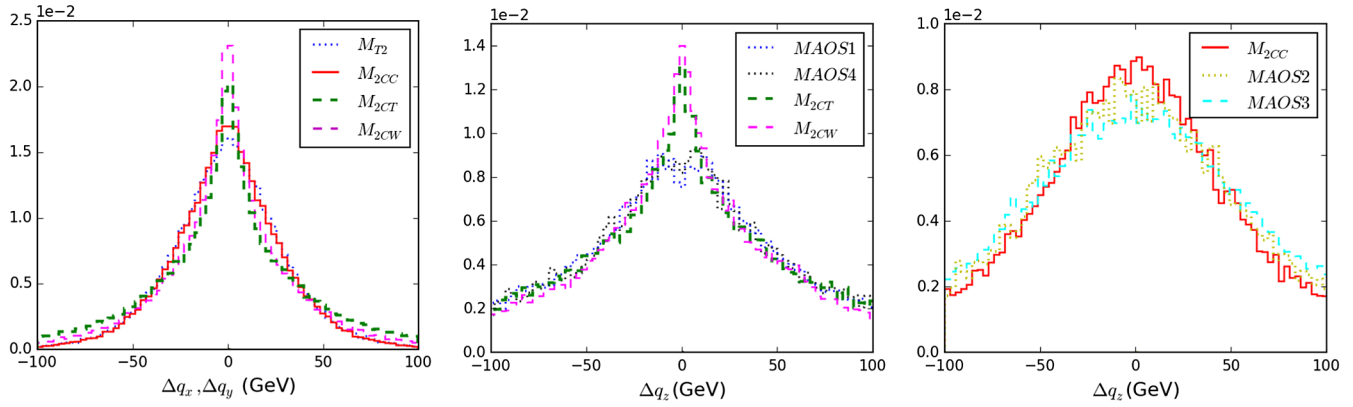
FIG. 2.   Difference between the reconstructed and the true values for the invisible momentum components in dilepton $t\bar{t}$ events. The left panel shows results from several methods for fixing the transverse components q_{ix} and q_{iy} by minimizing an invariant mass variable: $M_{T2}^{(b\ell)}$ (blue dotted line), $M_{2CC}^{(b\ell)}$ (red solid line), $M_{2Ct}^{(\ell)}$ (green dashed line) and $M_{2CW}^{(b\ell)}$ (magenta dashed line). The middle (right) panel shows corresponding results for the longitudinal components, obtained with methods which use (do not use) additional mass information: MAOS1$(b\ell;m_t)$ (blue dotted line), MAOS4$(b\ell;m_W)$ (black dotted line), $M_{2Ct}^{(\ell)}$ (green dashed line), $M_{2CW}^{(b\ell)}$ (magenta dashed line), $M_2A(b\ell)$ (red solid line), MAOS2$(b\ell;b\ell)$ (yellow dotted line) and MAOS3$(b\ell;b\ell)$ (cyan dashed line).

reconstruction, the transverse invisible components are obtained from M_{T2}, but this can be done for one of several possible subsystems, so we need to implement some notation to indicate which subsystem was used. For example, the abbreviation MAOS1$(b\ell;m_t)$ in Table I implies that the transverse invisible momenta were obtained from $M_{T2}^{(b\ell)}$, while the longitudinal invisible momenta were computed from the on-shell conditions for the parent particles (thus MAOS1) with mass m_t. Similarly, the abbreviation MAOS4$(\ell;m_t)$ indicates the use of $M_{T2}^{(\ell)}$ for fixing the transverse invisible momenta, then applying on-shell conditions for the top quarks, which in subsystem (ℓ) are relative particles (thus the name MAOS4). In both MAOS1 and MAOS4, the longitudinal momenta are obtained up to a four-fold ambiguity, as one has to solve a quadratic equation for each decay side.

(b) *Classic MAOS without mass information (MAOS2 and MAOS3).* There are two other MAOS schemes, which are applicable in the absence of any mass information about the parent or relative particles [51,63–65]. In MAOS2 one forces each parent mass to be equal to the computed M_{T2} value, i.e., $M_{P_i}(\vec{q}_i) = M_{T2}$, $i = 1, 2$, while in MAOS3 one demands that the parent mass be equal to the corresponding *transverse* parent mass obtained during the M_{T2} calculation: $M_{P_i}(\vec{q}_i) = M_{TP_i}(\vec{q}_{iT})$, $i = 1, 2$. Once again, each of these two MAOS schemes can be applied to any of the three possible subsystems [44]. Furthermore, in the previous step 1 we could in principle use a different

subsystem for the determination of the transverse invisible components, therefore now we need *two* subsystem labels to completely define the procedure. We shall employ the notation where the first subsystem label refers to the determination of the transverse invisible momenta, while the second subsystem label refers to the computation of the respective longitudinal components. For example, the abbreviation MAOS3$(\ell;b\ell)$ implies that the transverse components were obtained from $M_{T2}^{(\ell)}$, and then the longitudinal components were calculated from the MAOS3 condition for the parents in the $(b\ell)$ subsystem, i.e., the top quarks: $M_{t_i}(\vec{q}_i) = M_{Tt_i}(\vec{q}_{iT})$, $i = 1$, 2. The MAOS3 procedure always results in an unique ansatz, while MAOS2 is unique only for balanced events, i.e., events with $M_{TP_1} = M_{TP_2}$; for unbalanced events, MAOS2 gives exactly two solutions [55].

(v) *M_2-assisted invisible momentum reconstruction.* Another alternative is to use an M_2 variable— recall that the M_2 optimization procedure provides an ansatz for the full 3-vectors $\vec{q}_i$ of the invisible momenta. As indicated in Table I, such M_2-Assisted reconstructions will be denoted with M$_2$A and will carry a corresponding subsystem label as well.

(vi) *Hybrid methods.* The remaining methods in Table I are hybrid in the sense that they rely on a constrained M_{2CC} variable for obtaining the transverse components of the invisible momenta and on one of the MAOS methods for the determination of the longitudinal components. We shall call such methods CMAOS for
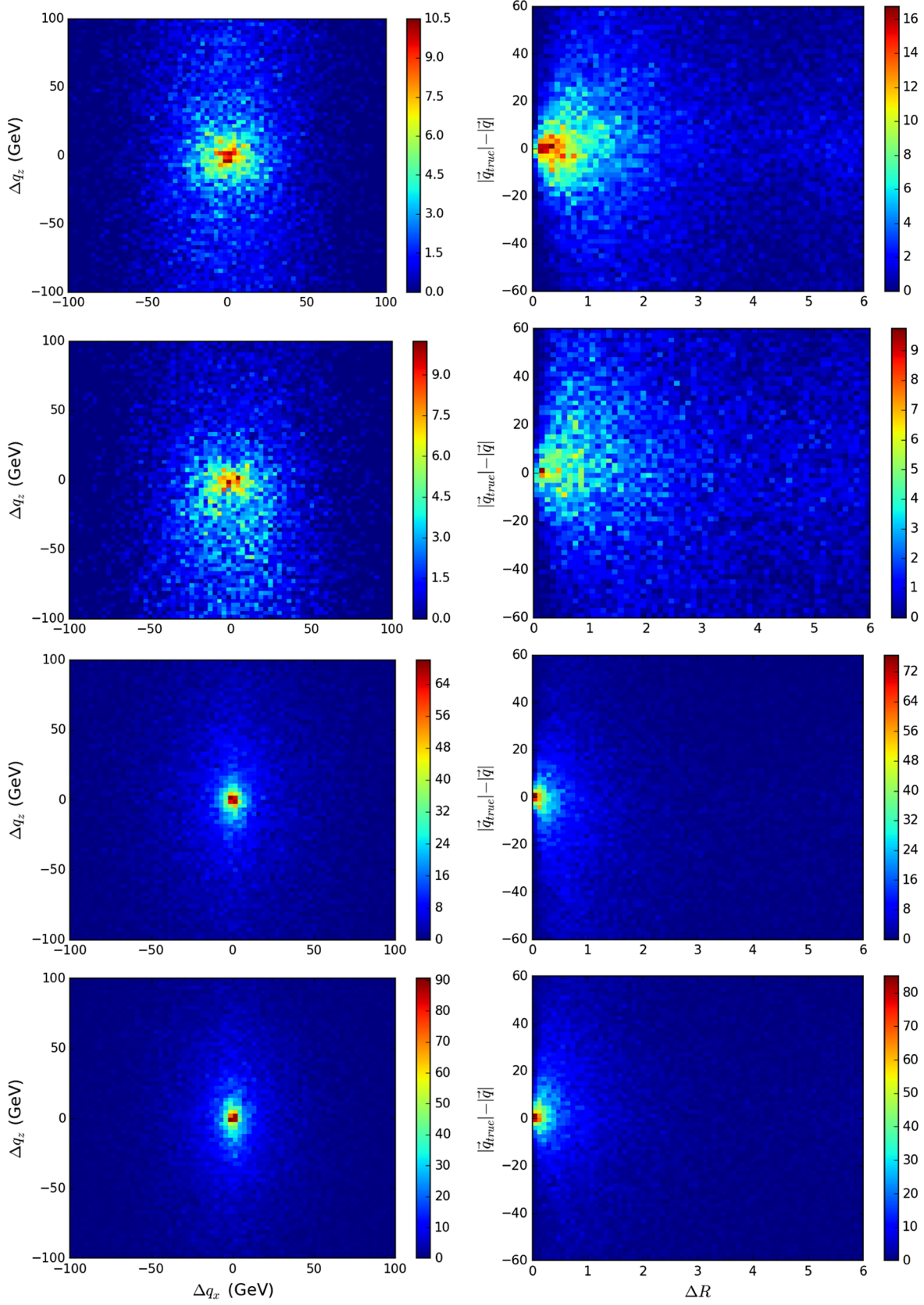
FIG. 3.   Correlations between Δq_z and Δq_x (left) and $|\vec{q}_{\text{true}}| - |\vec{q}|$ and $\Delta R(\vec{q}_{\text{true}}, \vec{q})$ (right) for four different schemes (from top to bottom): $\text{MAOS1}(b\ell; m_t)$, $\text{MAOS4}(b\ell; m_W)$, $M_{2Ct}^{(\ell)}$ and $M_{2CW}^{(b\ell)}$.
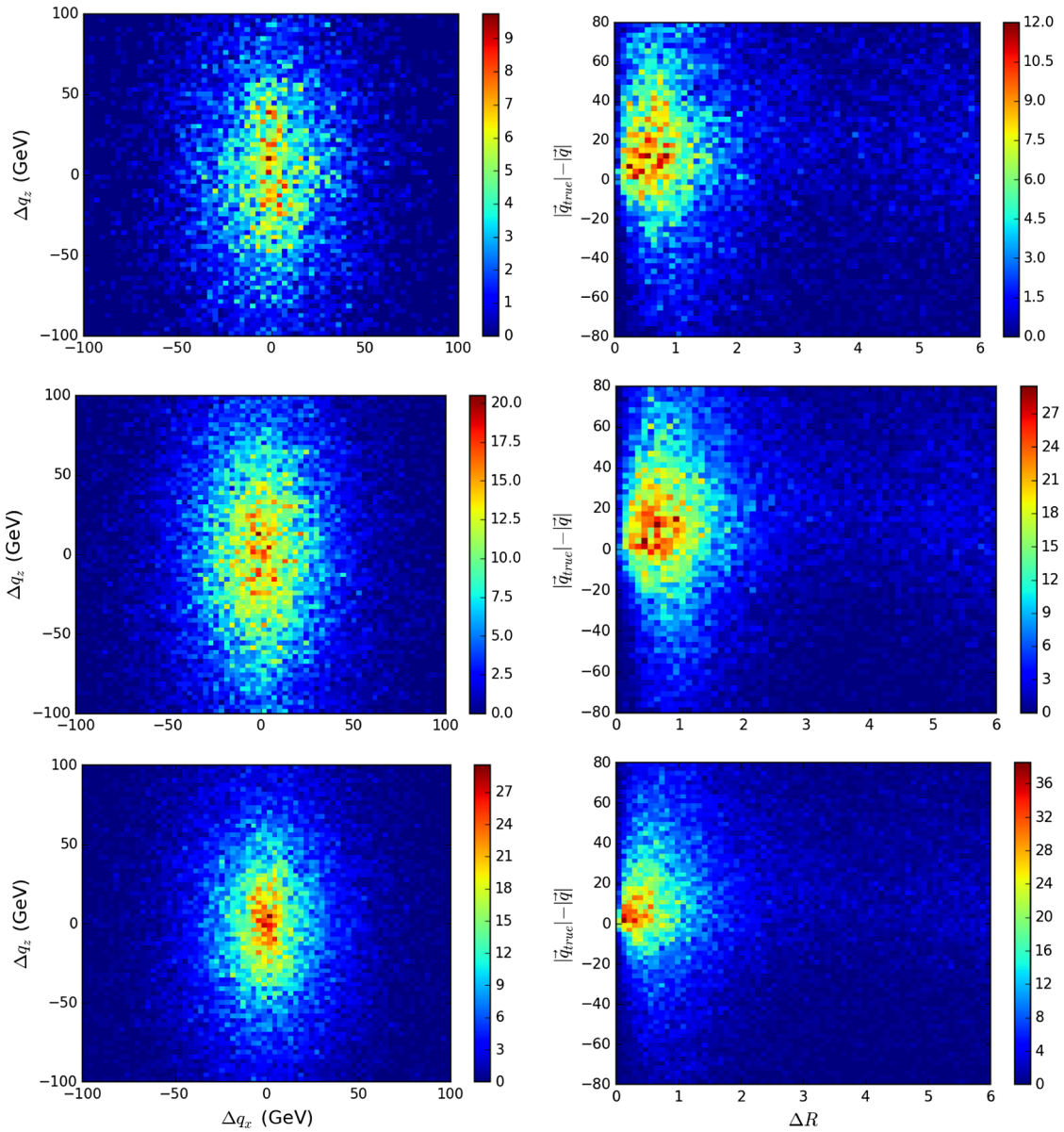
FIG. 4.   The same as Fig. 3, but for methods which do not use an extra mass input (from top to bottom): MAOS2($b\ell; b\ell$), MAOS3($b\ell; b\ell$) and M$_2$A($b\ell$).

"constrained" MAOS. The rationale for considering these methods is that, as we shall see below, the constrained M_{2CC} variables often provide superior ansätze for the transverse invisible momenta. Once again, one can "mix and match" the subsystems, which necessitates the use of two subsystem arguments for the CMAOS procedures listed in Table I.

Note that Table I does not include all logical possibilities—for example, in order to keep the table compact, we did not list the maximally constrained variables (11) and (12), which represent another M$_2$A option for simultaneously computing the transverse and longitudinal invisible components. One should also distinguish between methods

which use additional mass inputs (m_t or m_W) and methods which do not—in what follows, we shall be careful to compare the performance of those two categories of methods separately. For example, the methods in the yellow-shaded cells of Table I require an additional mass input and as such they will be discussed and contrasted in Table IX of Sec. IV C. On the other hand, the orange-shaded cells of Table I highlight a few representative methods which do not require additional mass inputs—those methods will be compared separately in Table XI of Sec. IV C. Note that the M$_2$A methods from Table I do not use extra mass information.

Having defined the different momentum reconstruction schemes, we are now in position to compare their

performance. Following [50,52], we shall first ask, how close each scheme gets to reproducing the *actual* values for the invisible momenta. Fig. 2 shows a comparison of the true values $\vec{q}_{\text{true}}$ of the transverse components (left panel) and the longitudinal components (middle and right panels) of the invisible momenta to the corresponding reconstructed values $\vec{q}$ obtained with different methods from Table I. The left panel in Fig. 2 contains the combined distributions of the transverse momentum differences $\Delta q_x \equiv q_{x,\text{true}} - q_x$ and $\Delta q_y \equiv q_{y,\text{true}} - q_y$ resulting from four different transverse momentum reconstruction schemes: $M_{T2}^{(b\ell)}$ (blue dotted line), $M_{2CC}^{(b\ell)}$ (red solid line), $M_{2Ct}^{(\ell)}$ (green dashed line) and $M_{2CW}^{(b\ell)}$ (magenta dashed line). In all four cases, the distributions are peaked at $\Delta q = 0$, which indicates that on average all four methods work rather well. We also observe that the distributions for $M_{2Ct}^{(\ell)}$ and $M_{2CW}^{(b\ell)}$, which utilize an extra mass input, are more sharply peaked, leading to much smaller errors. Among the two remaining distributions, $M_{2CC}^{(b\ell)}$ appears to perform slightly better than $M_{T2}^{(b\ell)}$.

The middle and right panels of Fig. 2 show similar plots for the longitudinal momentum difference $\Delta q_z \equiv q_{z,\text{true}} - q_z$, obtained with various methods for reconstructing the longitudinal invisible momenta: MAOS1$(b\ell; m_t)$ (blue dotted line), MAOS4$(b\ell; m_W)$ (black dotted line), $M_{2Ct}^{(\ell)}$ (green dashed line), $M_{2CW}^{(b\ell)}$ (magenta dashed line), M$_2$A$(b\ell)$ (red solid line), MAOS2$(b\ell; b\ell)$ (yellow dotted line) and MAOS3$(b\ell; b\ell)$ (cyan dashed line). Among the methods requiring an additional mass input (middle panel), $M_{2Ct}^{(\ell)}$ and $M_{2CW}^{(b\ell)}$ again work best, while among the more conservative methods (right panel), M$_2$A appears to outperform MAOS2 and MAOS3 (see also [44]).

Figures 3 and 4 provide a more detailed view of the results from Fig. 2 by showing the correlations between Δq_z and Δq_x (left panels) and between the difference in magnitudes $|\vec{q}_{\text{true}}| - |\vec{q}|$ and the direction mismatch $\Delta R(\vec{q}_{\text{true}}, \vec{q}) \equiv \sqrt{(\Delta \eta)^2 + (\Delta \varphi)^2}$ (right panels). Figures 3 and 4 reveal that in general, the transverse components of the invisible momenta are reconstructed more accurately than the longitudinal components, and that having additional mass information at one's disposal definitely helps. The right panels of Fig. 4 also show that for those methods, it is more likely to underestimate (than to overestimate) the magnitude of the invisible momentum—this is easy to understand for the case of events in which the two transverse invisible momenta partially cancel each other out in the $\vec{P}_T$ sum.

In conclusion of this section, we note that it is known that the performance of the methods with respect to invisible momentum reconstruction can be further improved by selecting only events near the kinematic endpoint of the respective invariant mass variable from which the ansatz

originated [44,50]. However, this benefit comes with a significant loss in statistics, and we shall not pursue this idea further here.

IV. CRITICAL REVIEW OF THE STANDARD METHOD

In this section, we analyze the standard method outlined in Refs. [36,53] for resolving the combinatorics problem in dilepton $t\bar{t}$ events. The method involves three steps, which were briefly reviewed in the Introduction, and will be now examined in detail in the following three subsections. For our numerical studies, we generate a partonic $t\bar{t}$ dilepton sample with 50k events, using the MadGraph5_aMC@NLO framework at the LHC with $\sqrt{s} = 14$ TeV center of mass energy and the default set of parton distribution functions [66]. The masses of the top quark and the W-boson are set to 173 GeV and 80.419 GeV, respectively, and we also take into account the proper finite widths—as we shall see below, this leads to the presence of events for which the top quarks and/or the W-bosons can be significantly off shell. In order to reduce the background, we apply the same basic cuts as those used in Ref. [53]. This leaves us with 18,456 events after cuts, for a cut efficiency of 37%. The different versions of the M_{T2} and M_2 kinematic variables will be computed with the OPTIMASS package [67].

A. Step I: $M_{T2}^{(b\ell)}$ and $m_{b\ell}$ cuts

The first step of the algorithm relies on the fact that in the event topology of Fig. 1, there exist several invariant mass variables, whose distributions exhibit an upper kinematic endpoint. If we choose the correct partition (9), all of these endpoints should be satisfied (barring off-shell effects). On the other hand, the wrong partition (10) may lead to one (or more) endpoint violations. The art of designing a good method for resolving the combinatorics lies in choosing the optimal invariant mass variables which will maximize the number of events for which the wrong partition (10) results in endpoint violations.

In principle, there are two types of invariant mass variables which can have kinematic endpoints:

(a) *Using visible particles from the same decay chain.* One can study the invariant mass of a collection of visible particles emerging from the same decay chain. For a long decay chain, there are many possible combinations [25], but for a short decay chain like the one in Fig. 1, the choice is unique—we can only form the two-body invariant mass of the b-jet and the lepton on each side. This gives us two values, $m_{b\ell^+}$ and $m_{\bar{b}\ell^-}$, each of which should obey the kinematic endpoint $m_{b\ell}^{\max}$, as illustrated in the left panel of Fig. 5. Following Refs. [36,53], we shall apply the stronger condition that the *larger* of these two values should also obey the upper kinematic endpoint:
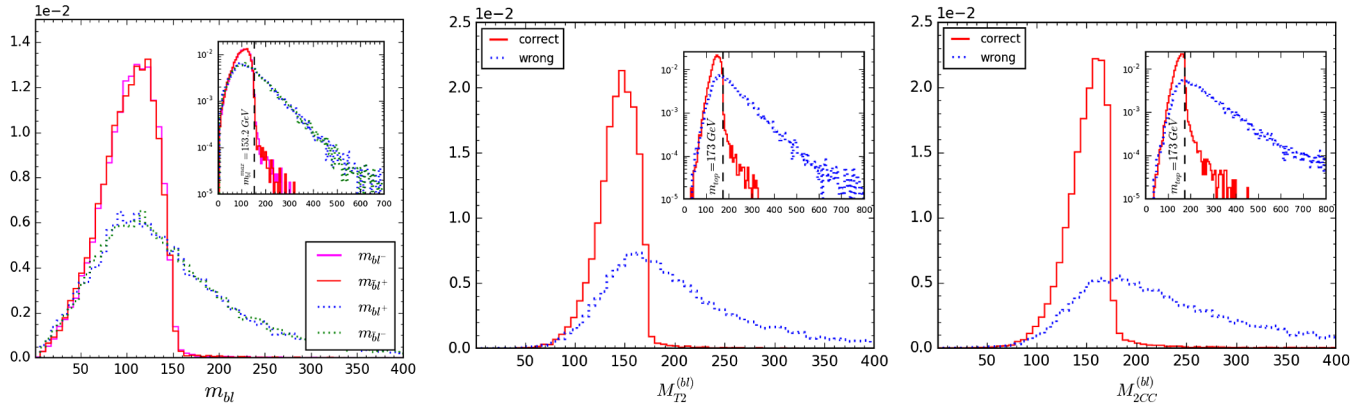
FIG. 5.   The distribution of $m_{b\ell}$ (left), $M_{T2}^{(b\ell)}$ (middle) and $M_{2CC}^{(b\ell)}$ (right) for the correct partition (9) (solid lines) and the wrong partition (10) (dotted lines). The inserts show a wider range of the x-axis and use a log scale for the y-axis. The corresponding M_{T2} and M_{2CC} distributions for the (b) and (ℓ) subsystems are shown in Fig. 9 below.

$$\max\{m_{b\ell^+}, m_{\bar{b}\ell^-}\} \leq m_{b\ell}^{\max}$$
$$\equiv \sqrt{\frac{(m_t^2 - m_W^2)(m_W^2 - m_\nu^2)}{m_W^2}}, \qquad (13)$$

where m_t, m_W and m_ν are respectively the masses of the top quark, the W-boson and the neutrino (we neglect the masses of the b-quark and the lepton). With their nominal values from the standard model, the endpoint is located at $m_{b\ell}^{\max} = 153.2$ GeV (see the insert in the left panel of Fig. 5).

(b) *Using visible particles from both decay chains.* The other possibility is to use the measured momenta of visible particles from both decay chains in order to construct invariant mass variables which also exhibit upper kinematic endpoints [8]. The prototypical example of such a variable is the Cambridge variable M_{T2} (see the middle panel in Fig. 5), but there are other possibilities as well, e.g., M_{CT} [68,69], M_{CT2} [70], and more recently, M_{2CC} [55] (see the right panel in Fig. 5). Following Refs. [36,53], we shall continue to consider M_{T2}, but we shall also entertain the possibility of using M_{2CC} instead. For the correct partition, the distributions of M_{T2} and M_{2CC} have common kinematic endpoints, and so the values of M_{T2} and M_{2CC} obey the hierarchy

$$M_{T2}^{(b\ell)} \leq M_{2CC}^{(b\ell)} \leq m_t, \qquad (14)$$

$$M_{T2}^{(\ell)} \leq M_{2CC}^{(\ell)} \leq m_W, \qquad (15)$$

where the endpoint values correspond to using the true[9] value of the neutrino mass $m_\nu = 0$. More

importantly, for the wrong partition, the shapes of the M_{T2} and M_{2CC} distributions are different (compare the blue dotted lines in the middle and right panels of Fig. 5), which will affect the efficiency for selecting the correct partition. Due to the general property (8), the wrong partition will still preserve the hierarchy $M_{T2} \leq M_{2CC}$, and therefore, the chances of endpoint violations will be increased if we were to use M_{2CC} in place of M_{T2} [61].

The distributions in Fig. 5 clearly motivate the use of the variables $m_{b\ell}$ and $M_{T2}^{(b\ell)}$ (or perhaps $M_{2CC}^{(b\ell)}$ instead) to resolve the two-fold combinatorial ambiguity.[10] This idea is implemented as Step I of the algorithm, by requiring that the invariant mass variables computed with a given partition P_i, $(i = 1, 2)$, obey the two kinematic endpoints (13) and (14). If one of the partitions obeys both endpoints, while the other does not, the former (latter) is declared to be the correct (wrong) partition P_C (P_W).

In order to quantify the discussion in the rest of paper, we introduce a simple Cartesian coordinate system designed to keep track of the kinematic endpoint violations (see Fig. 6). The x and y variables will be chosen so that their values are positive (negative) in the absence (presence) of a kinematic endpoint violation. To this end, we shall consider the difference between the value of the upper kinematic endpoint and the value of the variable itself—this difference is expected to be positive for the correct partition P_C, and conversely, if the difference is negative, it is likely that we have chosen the wrong partition P_W. Thus in Fig. 6 we choose the x-axis to be $m_t - M_{T2}^{(b\ell)}$ (later on we shall also consider $m_t - M_{2CC}^{(b\ell)}$), while for the y-axis we take $m_{b\ell}^{\max} - \max_j\{m_{b\ell}^{(j)}\}$, where $m_{b\ell}^{(1)}$ and $m_{b\ell}^{(2)}$ are the invariant

---

[9]If the neutrino mass were unknown, one could use any arbitrary value for the test daughter particle mass, and then extract the endpoint values in (14) and (15) from the data.

[10]For now, as in Refs. [36,53], we shall focus on the $(b\ell)$ subsystem, where one would expect the largest number of endpoint violations for the wrong kinematics [61]. The other two subsystems, (b) and (ℓ), will be discussed later in Sec. V A.
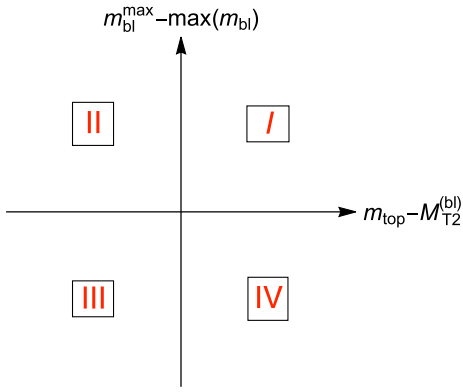
TABLE II. Resolving the combinatorial ambiguity at Step I. Each event is tagged with two quadrant numbers, one for each partition P_i. The quadrant number for the correct (wrong) combination is given in the 'row' ('column') label of the 4 by 4 matrix above. The green, red, and white fields indicate correctly resolved, wrongly resolved, and unresolved cases, respectively.

Quadrant for P_C	Quadrant for P_W			
	I	II	III	IV
I		🟩	🟩	🟩
II	🟥		🟩	
III	🟥	🟥		🟥
IV	🟥		🟩	

be the correct one (P_C). If both partitions fall in the same quadrant, then the event remains "unresolved" at Step I and we need to wait for the next steps of the algorithm. The situation becomes more complicated if both partitions fall outside quadrant I, and within different quadrants. In that case, we shall make the distinction between quadrant III, where both endpoints are violated, and quadrants II and IV, where there is a single endpoint violation. Correspondingly, if one partition falls in quadrant III while the other does not, the partition in quadrant III will be declared as the wrong partition (P_W). Finally, if one partition is in quadrant II while the other in quadrant IV, the event remains unresolved.

As a result of the application of Table III, each event will fall into one of two categories: resolved, for which one of the partitions P_k has been declared to be correct, and unresolved, for which no decision has been reached at that stage. Furthermore, the resolved events will not always be identified correctly—on occasion, the algorithm will mis-identify the wrong partition P_W as being the correct one. In order to better understand the power of each method below, we shall find it convenient to quote our results in the form of 4×4 tables like Table II, where we separately keep track of the quadrant for the correct partition P_C (indicated by the row label) and the quadrant for the wrong partition P_W (indicated by the column label). Each event will belong to one of the 16 boxes of Table II, and we will be interested in the number of events $N_{(I,J)}$ within each box, where the

TABLE III. Decision table for resolving the combinatorial ambiguity at Step I.

Quadrant for P_1	Quadrant for P_2			
	I	II	III	IV
I	unresolved	$P_C = P_1$	$P_C = P_1$	$P_C = P_1$
II	$P_C = P_2$	unresolved	$P_C = P_1$	unresolved
III	$P_C = P_2$	$P_C = P_2$	unresolved	$P_C = P_2$
IV	$P_C = P_2$	unresolved	$P_C = P_1$	unresolved

"quadrant indices" I (for the correct partition) and J (for the wrong partition) take values in the set $\{I, II, III, IV\}$. The action by Table III then causes all events within the green-shaded boxes of Table II to be *correctly* resolved, the events within the red-shaded boxes of Table II to be *wrongly* resolved, while the events within the unshaded boxes of Table II to remain *unresolved*. Then, for any given event sample, the total number N_C of correctly resolved events will be given by the total number of events within the green-shaded boxes of Table II:

$$N_C \equiv N_{(I,II)} + N_{(I,III)} + N_{(I,IV)} + N_{(II,III)} + N_{(IV,III)}. \tag{16}$$

Similarly, the total number of wrongly resolved events N_W will be equal to the total number of events within the red-shaded boxes of Table II:

$$N_W \equiv N_{(II,I)} + N_{(III,I)} + N_{(IV,I)} + N_{(III,II)} + N_{(III,IV)}. \tag{17}$$

Finally, the total number of unresolved events N_U is the sum of all events within the unshaded (white) boxes of Table II:

$$N_U \equiv N_{(I,I)} + N_{(II,II)} + N_{(III,III)} + N_{(IV,IV)}$$
$$+ N_{(II,IV)} + N_{(IV,II)}. \tag{18}$$

The algorithms below will be applied so that once an event is resolved, it does not get reclassified at a later stage, i.e., subsequent steps of the algorithm only affect the remaining unresolved events. Obviously, at different steps of the algorithms, the number of correctly resolved events (N_C), wrongly resolved events (N_W) and unresolved events (N_U) will vary, but those three numbers will always add up to the total number of events N_T in the sample:

$$N_T \equiv \sum_{I,J} N_{(I,J)} = N_C + N_W + N_U. \tag{19}$$

In order to compare different algorithms, we define the expected efficiency (sometimes called purity) as

$$\varepsilon = \frac{N_C + 0.5N_U}{N_C + N_U + N_W} = \frac{N_C + 0.5N_U}{N_T}. \tag{20}$$

For the purposes of calculating the efficiency, we shall assume that any unresolved events are eventually decided with a coin flip (50% efficiency).

Our results for $N_{(I,J)}$ are shown in Table IV, where the quadrants from Fig. 6 have been defined in terms of the variables $M_{T2}^{(b\ell)}$ and $m_{b\ell}$ (left 4×4 table) and the variables $M_{2CC}^{(b\ell)}$ and $m_{b\ell}$ (right 4×4 table). As expected, the most populated entries are found in the first rows, which

TABLE IV. Quadrant counts $N_{(I,J)}$ based on $M_{T2}^{(b\ell)}$ and $m_{b\ell}$ (left) and $M_{2CC}^{(b\ell)}$ and $m_{b\ell}$ (right) after the basic cuts. The corresponding efficiencies are 82% (left) and 85.3% (right).

Quadrant counts based on $M_{T2}^{(b\ell)}$ and $m_{b\ell}$					Quadrant counts based on $M_{2CC}^{(b\ell)}$ and $m_{b\ell}$				
Quadrant for P_C	Quadrant for P_W				Quadrant for P_C	Quadrant for P_W			
	I	II	III	IV		I	II	III	IV
I	6194	910	9793	1020	I	4494	2317	10222	217
II	22	31	106	5	II	168	178	480	5
III	29	10	191	4	III	37	26	251	1
IV	41	3	91	6	IV	17	3	38	2

confirms that in the case of the correct partition P_C, endpoint violations are relatively rare[11] We also find a handful of events in the off-diagonal boxes of the first column—for those events, off-shell effects caused the correct partition P_C to violate one or both of the kinematic endpoints, while the wrong partition P_W accidentally happened to satisfy both kinematic endpoints. Such events are problematic since they will be wrongly identified—one should keep in mind that only the symmetric combination of events $N_{(I,J)} + N_{(J,I)}$ is experimentally observable, since *a priori* we do not know which is the correct partition. Nevertheless, we observe that in the cases when one of the partitions ends up in quadrant I while the other does not, the large majority of the events will be correctly identified, since

$$N_{(I,II)} + N_{(I,III)} + N_{(I,IV)} \gg N_{(II,I)} + N_{(III,I)} + N_{(IV,I)}.$$

(21)

Another piece of good news is that whenever one of the partitions violates exactly one endpoint, while the other violates both, it is much more likely that the former (latter) is the correct (wrong) partition:

$$N_{(II,III)} \gg N_{(III,II)}; \qquad N_{(IV,III)} \gg N_{(III,IV)}. \quad (22)$$

Combining the relations (21) and (22) and using the definitions (16) and (17), we conclude that $N_C \gg N_W$, and therefore Step I of the method works relatively well.[12] With our definition for the efficiency (20), the classic method based on $M_{T2}^{(b\ell)}$ and $m_{b\ell}$ gives an efficiency of 82%. Looking back at the left side of Table IV, we see that for the standard method, the efficiency is hurt by the relatively large fraction of events which remain unresolved at this

stage—the unshaded boxes contain a total of $N_U = 6430$ events, or about 35% of the sample. The situation improves somewhat if we use the $M_{2CC}^{(b\ell)}$ variable instead of $M_{T2}^{(b\ell)}$: in that case, the right 4×4 table of Table IV contains fewer unresolved events ($N_U = 4933$, or only 27%), while the desired relations (21) and (22) are further enhanced. Both of these effects are responsible for increasing the efficiency (20) of the new $M_{2CC}^{(b\ell)}$ method to 85.3%. Note that in both methods, the majority of the unresolved events are found in the very first diagonal box (I, I), where both partitions are fully consistent with the kinematics of the assumed event topology. This is why, in what follows we shall focus our attention on the additional steps of the algorithm which can successfully classify the remaining unresolved events, especially those in the (I, I) box.

B. Step II: The presence of complex solutions

In the second step of the method, one attempts to reconstruct the longitudinal momenta of the invisible particles, by enforcing on-shell conditions for a parent particle (MAOS1) or for a relative particle (MAOS4). Since the on-shell conditions result in quadratic equations, the solutions are not guaranteed to be real. The idea of Step II is to compare the two possible partitions P_k in terms of the number of complex solution pairs $\mathbb{C}$ for the longitudinal momenta. Since there is a separate calculation for each decay chain, there are three possible outcomes:

(a) $\mathbb{C} = 0$. Both decay chains result in real solutions.
(b) $\mathbb{C} = 1$. Exactly one decay chain gives a pair of complex solutions, while the other decay chain has real solutions.
(c) $\mathbb{C} = 2$. Both decay chains result in complex solutions.

For the purposes of applying Step II of the method, there is no need to distinguish between the cases of $\mathbb{C} = 1$ and $\mathbb{C} = 2$, since the important point is simply that $\mathbb{C} > 0$. The action of Step II is the following: if one of the partitions P_k gives $\mathbb{C} = 0$, while the other has $\mathbb{C} > 0$, then the former (latter) partition is declared to be the correct (wrong) one.

---

[11]As a sanity check, we have verified that if we turn off the width effects by hand, by forcing both the top quarks and the W-bosons on shell, all entries in the second through fourth rows are exactly zero.

[12]This can also be seen directly by comparing the green-shaded and the red-shaded boxes of Table IV.

TABLE V. Classification of events according to the complexity of the solutions for the longitudinal invisible momenta in the case of MAOS1($b\ell; m_t$), i.e., the transverse momenta of the neutrinos are fixed during the minimization of $M_{T2}^{(b\ell)}$, while the longitudinal components are obtained from the on-shell conditions for the top quarks on each side. The table is organized by quadrant counts $N_{(I,J)}$ as in Table IV. For each (I, J) quadrant pair, we further classify the events according to the number of decay sides $\mathbb{C}$ with complex solutions for the longitudinal momenta, and the table lists the corresponding values of $N_{(I,J)}^{(\mathbb{C})}$. This is done separately for the correct partition P_C (upper rows) and for the wrong partition P_W (lower rows).

	I			II			III			IV			
	0	1	2	0	1	2	0	1	2	0	1	2	$\mathbb{C}$
I	6194	0	0	910	0	0	9793	0	0	1020	0	0	P_C
	6194	0	0	0	1	909	0	7215	2578	1020	0	0	P_W
II	0	2	20	0	0	31	0	2	104	0	0	5	P_C
	22	0	0	0	0	31	0	69	37	5	0	0	P_W
III	0	22	7	0	5	5	0	124	67	0	4	0	P_C
	29	0	0	0	0	10	0	138	53	4	0	0	P_W
IV	41	0	0	3	0	0	91	0	0	6	0	0	P_C
	41	0	0	0	0	3	0	66	25	6	0	0	P_W

TABLE VI. The same as Table V, but for the case of MAOS4($b\ell; m_W$), i.e., the transverse momenta of the neutrinos are still obtained from the minimization of $M_{T2}^{(b\ell)}$, but now the longitudinal components are computed from the on-shell conditions for the W-bosons instead.

	I			II			III			IV			
	0	1	2	0	1	2	0	1	2	0	1	2	$\mathbb{C}$
I	5005	1086	103	582	299	29	8245	1497	51	908	109	3	P_C
	4094	2074	26	136	751	23	3893	5817	83	661	359	0	P_W
II	7	14	1	12	16	3	58	46	2	2	3	0	P_C
	9	13	0	5	24	2	26	79	1	1	4	0	P_W
III	12	17	0	5	5	0	84	106	1	3	1	0	P_C
	22	7	0	3	6	1	96	95	0	3	1	0	P_W
IV	36	5	0	3	0	0	78	13	0	6	0	0	P_C
	31	10	0	1	2	0	58	33	0	6	0	0	P_W

As already discussed in Sec. III, there are several ways to implement the MAOS idea and compute longitudinal invisible momenta. Tables V and VI show results for the cases of MAOS1($b\ell; m_t$) and MAOS4($b\ell; m_W$), respectively.[13] Similarly to Table IV, each table is organized by quadrants, and within each cell (I, J) we show the number of events $N_{(I,J)}^{(\mathbb{C})}$ with a given value of $\mathbb{C}$, for the correct partition (upper rows) and the wrong partition (lower rows).

Let us first focus on Table V, which shows several interesting trends. First, recall the motivation behind

Step II—one was hoping to find that the correct partition P_C would always give real solutions ($\mathbb{C} = 0$), while the wrong partition P_W would always lead to complex solutions ($\mathbb{C} > 0$). Table V reveals that this expectation is indeed true, but only for certain quadrant pairs: (I, II), (I, III), (IV, II) and (IV, III). For those cases, Step II would be able to perfectly resolve the combinatorial ambiguity, and it seems that the method works as designed. Unfortunately, three out of these four quadrant pairs are already shaded in green (see Table II), which means that those events were already perfectly resolved by Step I, thus the additional benefit from Step II for those three quadrant pairs is exactly zero. As for the fourth quadrant pair, (IV, II), it is very sparsely populated, and furthermore, any

---

[13]The former was the method used in Ref. [53], but the latter is in principle a viable option as well.

TABLE VII.   The same as Table V, but for the case of CMAOS1$(b\ell; m_t)$, i.e., the transverse momenta of the neutrinos are now fixed from the minimization of $M_{2CC}^{(b\ell)}$ instead of $M_{T2}^{(b\ell)}$, and then the longitudinal components are again obtained from the on-shell conditions for the top quarks on each side. Here the quadrants are defined in terms of $M_{2CC}^{(b\ell)}$ and $m_{b\ell}$ and correspond to the right 4×4 table in Table IV.

	I			II			III			IV			
	0	1	2	0	1	2	0	1	2	0	1	2	$\mathbb{C}$
I	4494	0	0	2317	0	0	10222	0	0	217	0	0	P_C
	4494	0	0	348	729	1240	62	5482	4678	217	0	0	P_W
II	62	70	36	63	64	51	184	168	128	2	1	2	P_C
	168	0	0	21	53	104	4	211	265	5	0	0	P_W
III	2	20	15	4	9	13	7	138	106	0	1	0	P_C
	37	0	0	3	7	16	0	150	101	1	0	0	P_W
IV	17	0	0	3	0	0	38	0	0	2	0	0	P_C
	17	0	0	0	1	2	0	25	13	2	0	0	P_W

benefit there would be offset by the negative effects from the symmetric case of (II, IV), where the results are contrary to our expectations above—now it is the correct partition P_C which leads to complex solutions.[14] [The same phenomenon is observed for the other three symmetric pairs as well—see the red-shaded boxes corresponding to (II, I), (III, I), and (III, IV), where it is again the correct partition P_C which has $\mathbb{C} > 0$.]

Thus we conclude that for the events which were already resolved at Step I (the green-shaded and red-shaded cells in Table V), Step II does not bring anything new—its results are either fully correlated with Step I [as for the quadrant pairs (I, II), (I, III) and (IV, III) and their red-shaded symmetric partners on the other side of the diagonal], or inconclusive, since the two partitions behave identically (e.g., for quadrant pairs (I, IV) and (II, III) and their partners]. Therefore, we need to concentrate on the unresolved events in the unshaded cells in Table V, since those were precisely the events which Step II was meant to address. Unfortunately, we observe that in the unshaded cells along the diagonal in Table V, the two partitions lead to the same result and cannot be discriminated, while the remaining two cells (II, IV) and (IV, II) were already discussed above—their statistics is too low, and they tend to cancel each other out, thus they will not appreciably affect the overall efficiency.

Based on the results from Table V, we conclude that if one were to apply Step II based on the MAOS1$(b\ell; m_t)$ method, which was used in Ref. [53], there would be no

additional benefit beyond Step I, and therefore Step II is unnecessary and can be eliminated. However, this still leaves open the question whether some modified version of Step II can still be useful, e.g., applying a different MAOS scheme like MAOS4$(b\ell; m_W)$ (see Table VI), or perhaps using one of the CMAOS schemes based on the M_{2CC} variables (see Tables VII and VIII). But before we discuss these options, it will be useful to understand the results from Table V from a physics point of view. A careful inspection of Table V reveals that its content can be summarized as follows: for any partition P_k, quadrants I and IV produce only real solutions, while quadrants II and III lead to only complex solutions. This means that the existence of complex solutions is correlated with the x-axis variable of Fig. 6 ($M_{T2}^{(b\ell)}$), and not with the y-axis variable ($m_{b\ell}$). This is easy to understand: $m_{b\ell}$ is formed from visible particle momenta only, and is not directly related to any invisible momenta. Therefore, a violation of the $m_{b\ell}$ kinematic endpoint by itself does not imply unphysical invisible momenta. On the other hand, the physical meaning of $M_{T2}^{(b\ell)}$ is the lowest possible mass of the parent particle, in this case the top quark. If the value of $M_{T2}^{(b\ell)}$ strictly violates the kinematic endpoint m_t, i.e., $M_{T2}^{(b\ell)} > m_t$, then enforcing the on-shell condition for the top quark will necessarily result in unphysical (complex) values for the momenta. In particular, quadrants II and III, in which the $M_{T2}^{(b\ell)}$ endpoint is violated by definition, will always produce complex momenta.

While the above logic helps to understand the results from Table V, it does not carry over directly to the case of MAOS4$(b\ell; m_W)$ shown in Table VI, since now we are enforcing an on-shell condition for a different (relative) particle. The trends which we previously observed in Table V are still noticeable, but they are not so clear cut.

---

[14]The fact that the correct partition P_C may result in complex momenta should not be surprising—this can be due to finite width and off-shell effects. As a sanity check, we have verified that in the zero-width limit only the first row in Table V has any nonzero entries, while the second, third and fourth rows are empty.

TABLE VIII. The same as Table VI, but for the case of CMAOS4($b\ell$; m_W), i.e., the transverse momenta of the neutrinos are now obtained from the minimization of $M_{2CC}^{(b\ell)}$, then the longitudinal components are computed from the on-shell conditions for the W-bosons as before.

	I			II			III			IV			
	0	1	2	0	1	2	0	1	2	0	1	2	$\mathbb{C}$
I	3840	497	157	1810	385	122	9089	931	202	214	3	0	P_C
	3652	612	230	397	879	1041	3005	3132	4085	217	0	0	P_W
II	52	66	50	65	84	29	228	194	58	1	2	2	P_C
	113	37	18	30	81	67	121	143	216	5	0	0	P_W
III	14	13	10	11	9	6	101	76	74	1	0	0	P_C
	33	3	1	10	11	5	90	88	73	1	0	0	P_W
IV	17	0	0	3	0	0	38	0	0	2	0	0	P_C
	17	0	0	1	0	2	18	12	8	2	0	0	P_W

Nevertheless, if we focus on the unresolved events after Step I (the unshaded cells in Table VI), we again see that Step II does not do particularly great on those events. The largest effect is in the (I, I) cell, where the efficiency for resolving the correct partition is 57.4%, which is slightly better than a coin flip. Adding up the results from all previously unresolved cells, we find that if we were to perform Step II with the MAOS4($b\ell$; m_W) version of the method instead of the MAOS1($b\ell$; m_t) option used in Ref. [53], the overall efficiency would increase to 84.5%, which is still worse than the result (85.3%) found in Sec. IV A with the improvements in Step I alone, taking advantage of $M_{2CC}^{(b\ell)}$ (see the right 4×4 table in Table IV).

Tables VII and VIII show results from two similar exercises where we use the corresponding CMAOS methods, i.e., fixing the transverse components of the invisible momenta from $M_{2CC}^{(b\ell)}$ instead of $M_{T2}^{(b\ell)}$, then applying the on-shell conditions for the parent (top quark) or relative (W-boson) particle. As shown previously in Figs. 2–4, the $M_{2CC}^{(b\ell)}$ variable generally provides a more accurate estimate of the individual transverse momentum components for the invisible particles, and one might hope that incorporating $M_{2CC}^{(b\ell)}$ somehow into the Step II algorithm would improve the performance. However, Table VII shows that the improvement in the case of CMAOS1($b\ell$; m_t) is very marginal—the efficiency increases from 85.3% after Step I to 85.4% after Step II. The effect is slightly better in Table VIII, which uses the CMAOS4($b\ell$; m_W) option—there the efficiency increases from 85.3% after Step I to 85.9% after Step II. However, even this increase is too small to justify the presence of Step II—as we shall see later on, there exist other, much more effective techniques. Therefore, as a final summary of this subsection, we conclude that Step II can be safely dropped altogether, since its results are largely correlated with Step I.

C. Step III and possible variations

In this subsection we shall discuss different possible options for the third step of the method and investigate their performance. To recap the situation: when we used $M_{T2}^{(b\ell)}$ and $m_{b\ell}$ at Step I, we ended up with $N_C = 11,\,920$ correctly resolved events, $N_W = 106$ incorrectly resolved events, and $N_U = 6,\,430$ unresolved events, for an efficiency of 82% (see the top of the middle column in Table IX). If, on the other hand, we choose to use $M_{2CC}^{(b\ell)}$ and $m_{b\ell}$ at Step I, we obtain $N_C = 13,\,274$ correctly resolved events, $N_W = 249$ incorrectly resolved events, and $N_U = 4,\,933$ unresolved events, for an efficiency of 85.3% (see the top of the right column in Table IX). Then in Sec. IV B we showed that Step II does not add much and can be ignored. This brings us to Step III, whose purpose is to further classify the remaining unresolved events after Step I (6,430 and 4,933, respectively) on a statistical basis, using suitable discriminating variables.

We begin by reviewing the method suggested in Ref. [53], which introduced several kinematic variables, T_i, $i = 1, \ldots, 4$. These variables were designed so that their values tend to be *larger* for the case of the wrong partition, i.e.,

$$T_i(P_W) > T_i(P_C). \tag{23}$$

While it is not guaranteed that (23) will be true in every single event, if it holds for the majority of the events, one can attempt to identify the correct partition P_C by declaring [53]

$$P_C = \begin{cases} P_1, & \text{if } \Delta T_i(P_2, P_1) > 0; \\ P_2, & \text{if } \Delta T_i(P_2, P_1) < 0; \end{cases} \tag{24}$$

where

$$\Delta T_i(P_2, P_1) \equiv T_i(P_2) - T_i(P_1). \tag{25}$$

In the case of several good variables T_i, one can generalize (24) by choosing the correct partition P_C to be the partition

TABLE IX. Efficiencies for selecting the correct partitioning [as defined in Eq. (20)] for several different procedures which use the known values of the top mass m_t or the W-boson mass m_W.

	Algorithm for Step I					
	$M_{T2}^{(b\ell)}$ and $m_{b\ell}$			$M_{2CC}^{(b\ell)}$ and $m_{b\ell}$		
	Correct	Wrong	Unresolved	Correct	Wrong	Unresolved
Step I: Quadrant counts	11,920	106	6,430	13,274	249	4,933
efficiency	$\varepsilon = 82.0\%$			$\varepsilon = 85.3\%$		
Remaining unresolved events	6,430			4,933		
ΔT_i method	3,445	1,573	1,412	2,820	1,462	651
cumulative efficiency	$\varepsilon = 87.1\%$			$\varepsilon = 89\%$		
ΔT_2 type cut alone	3,160	3,270	—	2,426	2,507	—
cumulative efficiency	$\varepsilon = 81.7\%$			$\varepsilon = 85.1\%$		
ΔT_3 and ΔT_4 alone	4,101	1,624	705	2,868	1,328	737
cumulative efficiency	$\varepsilon = 88.7\%$			$\varepsilon = 89.5\%$		
m_t^{reco} with MAOS4($b\ell;m_W$)	2,392	1,371	2,667	2,212	1,238	1,483
cumulative efficiency	$\varepsilon = 84.8\%$			$\varepsilon = 87.9\%$		
m_t^{reco} with MAOS1($\ell;m_W$)	4,186	2,188	56	3,033	1,860	40
cumulative efficiency	$\varepsilon = 87.4\%$			$\varepsilon = 88.5\%$		
m_t^{reco} with CMAOS4($b\ell;m_W$)	2,262	1,307	2,861	2,122	1,228	1,583
cumulative efficiency	$\varepsilon = 84.6\%$			$\varepsilon = 87.7\%$		
m_t^{reco} with CMAOS1($\ell;m_W$)	2,995	1,790	1,645	2,565	1,617	751
cumulative efficiency	$\varepsilon = 85.3\%$			$\varepsilon = 87.9\%$		
m_W^{reco} with MAOS1($b\ell;m_t$)	4,344	1,856	230	3,044	1,546	343
cumulative efficiency	$\varepsilon = 88.8\%$			$\varepsilon = 89.3\%$		
m_W^{reco} with MAOS4($\ell;m_t$)	1,627	792	4,011	1,505	760	2,688
cumulative efficiency	$\varepsilon = 84.3\%$			$\varepsilon = 87.3\%$		
m_W^{reco} with CMAOS1($b\ell;m_t$)	3,328	1,583	1,519	3,044	1,459	430
cumulative efficiency	$\varepsilon = 86.7\%$			$\varepsilon = 89.6\%$		
m_W^{reco} with CMAOS4($\ell;m_t$)	1,922	947	3,561	1,870	928	2,135
cumulative efficiency	$\varepsilon = 84.7\%$			$\varepsilon = 87.3\%$		

P_1 (P_2) if the *majority* of the quantities $\Delta T_i(P_2, P_1)$ are positive (negative). In the following, we shall refer to this procedure as the "ΔT_i method" [53].

The T_i variables considered in Ref. [53] were the following:

$$T_1(P_k) \equiv \max_j \{m_{b\ell}^{(j)}\}(P_k), \qquad (26)$$

$$T_2(P_k) \equiv M_{T2}^{(b\ell)}(P_k), \qquad (27)$$

$$T_3(P_k) \equiv \sum_{\substack{j=1,2; \\ \alpha=+,-}} |m_t^{reco}(j,\alpha) - m_t|(P_k), \qquad (28)$$

$$T_4(P_k) \equiv \sum_{\substack{j=1,2; \\ \alpha=+,-}} |m_W^{reco}(j,\alpha) - m_W|(P_k), \qquad (29)$$

where P_k is one of two partitions and the index j labels the two decay chains in Fig. 1. The variable m_t^{reco} (m_W^{reco}) is the reconstructed mass of the top quark (the W-boson) with a MAOS-type method which uses the W-boson mass (the top mass) as an input. Since the longitudinal invisible momenta are obtained from a quadratic equation, in general there are two solutions, labeled by $\alpha = \pm$, corresponding to the two signs in front of the discriminant. Thus in each event one can obtain four reconstructed top quark masses, $m_t^{reco}(j, \alpha)$, and four reconstructed W-boson masses, $m_W^{reco}(j, \alpha)$. The

TABLE X. Breakdown of the events from Table IX which remained unresolved after Step I (6,430 and 4,933, respectively). The table shows the effect of applying the ΔT_i method at Step III, for the case of $T_2 = M_{T2}^{(b\ell)}$ (left) and $T_2 = M_{2CC}^{(b\ell)}$ (right). The resulting cumulative efficiencies are 87.1% and 89%, as shown in Table IX.

	Algorithm for Step I						
	$M_{T2}^{(b\ell)}$ and $m_{b\ell}$				$M_{2CC}^{(b\ell)}$ and $m_{b\ell}$		
Quadrants with unresolved events	Total	C	W	U	Total	C	W	U
(I, I)	6,194	3,266	1,521	1,407	4,494	2,471	1,308	715
(II, II)	31	26	5	⋯	178	147	26	5
(III, III)	191	149	37	5	251	185	55	11
(IV, IV)	6	1	5	⋯	2	0	2	⋯
(II, IV) ⊕ (IV, II)	8	3	5	⋯	8	3	3	2
Total after Step III	6,430	3,445	1,573	1,412	4,933	2,820	1,462	651

idea behind the T_3 and T_4 variables in (28) and (29) is to compare those reconstructed values to the true values m_t and m_W, respectively. For the correct partition P_C, on average one might expect to find the reconstructed values closer to the true ones, in agreement with (23).

In Table IX we test several options for discrimination variables which can be applied at Step III. Our benchmark is the ΔT_i method of Ref. [53], which made use of only three variables, T_2, T_3 and T_4, since the fourth one, T_1, was found to be significantly correlated with T_2. For consistency, whenever the quadrants from Step I are defined in terms of $M_{2CC}^{(b\ell)}$ (right column in Table IX), we shall replace (27) with $T_2 = M_{2CC}^{(b\ell)}$. Table IX reports results from both versions of the ΔT_i method—we see that the overall efficiency can be further improved to 87.1% and 89%, respectively. The observed improvement at Step III is due to correctly categorizing (at the rate of about 2:1) the majority of the remaining unresolved events—see Table X, which gives the breakdown among the individual "unresolved" cases from Table III. In spite of this progress, we also notice that a certain number of events (1,412 and 651, correspondingly) still remain unresolved. At first glance, this seems odd, since the ΔT_i method uses an odd number of variables, so for each event, there should be a clear winner between the two candidate partitions P_1 and P_2. However, recall that the longitudinal momentum reconstruction sometimes results in complex solutions, in which case the corresponding variable T_3 or T_4 is undefined.[15] Thus the remaining unresolved events after Step III are those where only two of the three T_i variables were calculated, and each preferred a different partition P_k.

Table X demonstrates that Step III was relatively successful. Nevertheless, in the remainder of this section we shall investigate whether further improvements at the level of Step III are still possible. Let us begin by studying the benefit from each individual variable, T_2, T_3 and T_4,

used in the ΔT_i algorithm. Following Ref. [53], in Fig. 8 we show distributions of the "ordered" differences

$$\Delta T_i(P_W, P_C) \equiv T_i(P_W) - T_i(P_C) \qquad (30)$$

for the three variables T_2 (left panels), T_3 (middle panels) and T_4 (right panels), where we use MC truth information to make sure that we subtract the variables in the order indicated in (30). For the plots in the top (bottom) row of Fig. 8, the transverse invisible momenta were obtained with the help of the $M_{T2}^{(b\ell)}$ ($M_{2CC}^{(b\ell)}$) variable. Plotting in terms of the ordered difference (30) is very useful, since it allows us to see how often the expected relationship (23) holds: the difference (30) is positive (negative) if (23) is satisfied (violated). Thus, by applying the prescription (24) for a given variable T_i, we shall correctly resolve all events with positive values of $\Delta T_i(P_W, P_C)$ (the shaded portions of the distributions in Fig. 8), and we shall wrongly resolve the events with negative values of $\Delta T_i(P_W, P_C)$ (the unshaded portions of the distributions in Fig. 8). By comparing the areas of the shaded and unshaded portions of each distribution, we can judge the discrimination power of each variable. For example, the left panels in Fig. 8 show that when considering the whole event sample (red histograms), T_2 appears to be a good variable, since as many as 79% of the events have positive values of $\Delta T_2(P_W, P_C)$ [53]. Unfortunately, we find that this conclusion is invalidated after the application of Step I—for the remaining unresolved events after Step I (the blue histograms in Fig. 8), it is actually more likely to find a negative value of $\Delta T_2(P_W, P_C)$ instead, thus obtaining the wrong answer for P_C. This observation reveals that the results from Step I and Step III are also somewhat correlated—the events which are easy to analyze with T_2 at Step III would already be correctly resolved at Step I. Using ΔT_2 alone (without ΔT_3 or ΔT_4) in fact lowers the cumulative efficiency, as shown in Table IX. This motivates us to drop ΔT_2 from further consideration and repeat Step III *without* ΔT_2, i.e., with only ΔT_3 and ΔT_4. As shown in Table IX, this leads to a slight

---

[15]This will become more evident when inspecting the normalization of the plots in Fig. 8 below.
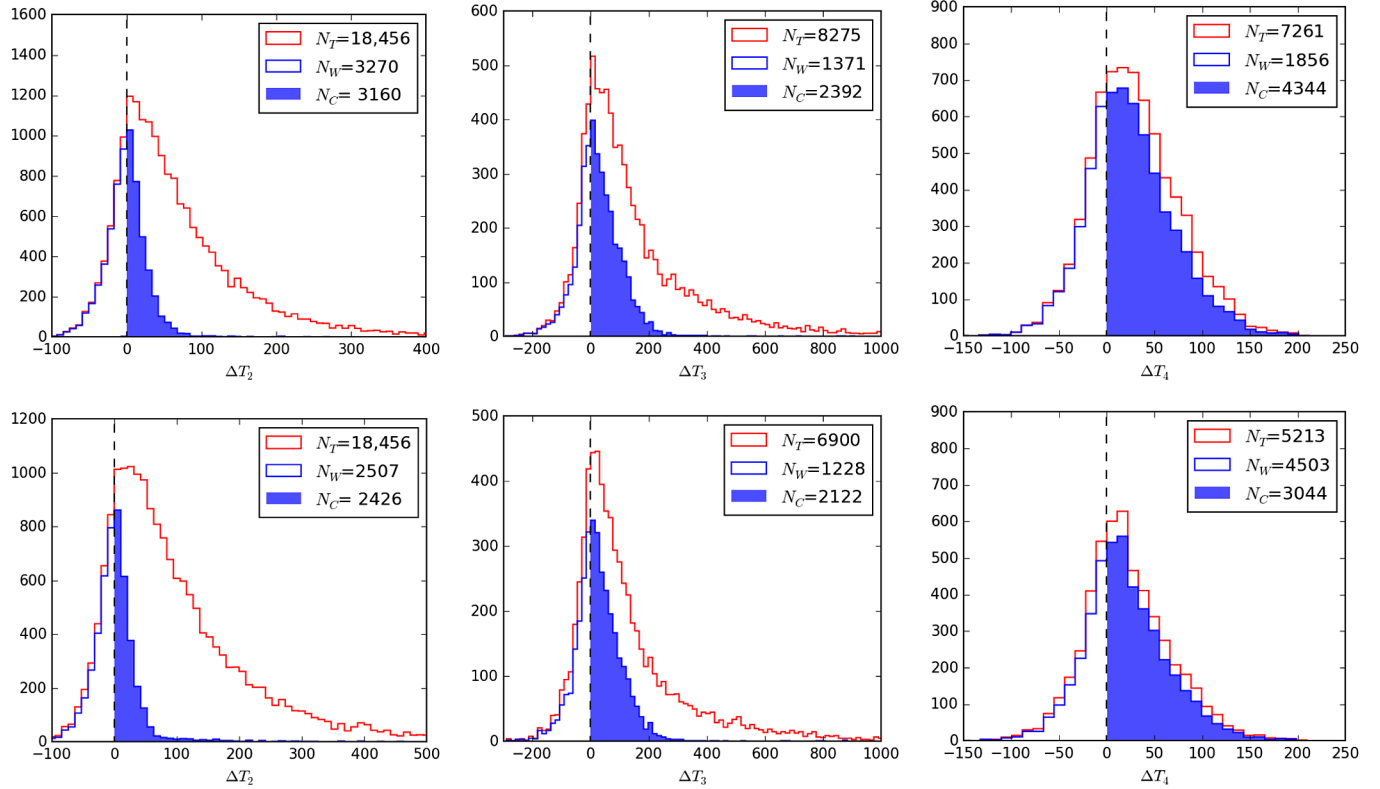
FIG. 8.   Distributions of the ordered differences (30) for T_2 (left), T_3 (middle) and T_4 (right). The red distributions show all events while the blue distributions only include the events which remain unresolved after Step I. For the MAOS-type plots in the top row, the transverse invisible momenta were obtained with the help of $M_{T2}^{(b\ell)}$, while for the CMAOS-type plots in the bottom row the transverse invisible momenta were fixed from $M_{2CC}^{(b\ell)}$. In the middle and right panels we only plot events with real solutions for the longitudinal momenta. The shaded (unshaded) portions of the histograms represent events which will be correctly (incorrectly) resolved with that particular ΔT_i variable alone.

improvement of the cumulative efficiency, to 88.7% and 89.5%, respectively, indicating that T_3 and T_4 retain some discrimination power even after Step I (this can also be deduced from the blue histograms in the middle and right panels of Fig. 8).

Given the large variety of MAOS and CMAOS methods described in Sec. III (see Table I), next we check if there exist alternative versions of the T_3 and T_4 variables which are better suited for our purpose. In the remainder of Table IX we study the effect on the cumulative efficiency if the reconstruction is performed with one of the eight yellow-shaded methods from Table I. Taking one variable at a time, we apply Step III as in (24) and quote the resulting cumulative efficiency in the last 8 rows of Table IX. The results are rather illuminating, and indicate that "not mixing" the subsystems provides the best option for constructing a useful T_i variable. For example, when the transverse invisible components are fixed with the help of the $(b\ell)$ subsystem, in which the top quark is the parent particle, then we are better off applying the on-shell condition on the *same* particle in order to reconstruct the longitudinal invisible momenta. Similarly, if the transverse momenta are obtained from the (ℓ) subsystem, in which the

W-boson is the parent particle, then it is preferable to apply the on-shell condition on the W-boson as well. For both MAOS and CMAOS reconstructions, Table IX shows that the highest efficiencies are obtained in the case of $(b\ell, m_t)$ and (ℓ, m_W) type variables. It is interesting to note that the performance of the modified method above (which used only ΔT_3 and ΔT_4) can be matched and even slightly exceeded by using a single additional variable at Step III, provided that we pick the right one: the MAOS1$(b\ell; m_t)$ option gives 88.8% (compare to 88.7% before), while CMAOS1$(b\ell; m_t)$ yields 89.6% (compare to 89.5%).

Another interesting point is that in all cases, the cumulative efficiencies in the right column of Table IX are higher than those in the middle column, thus reinforcing the idea of using the constrained M_{2CC} variables. In Sec. IV A we already established that it is beneficial to redefine Step I in terms of M_{2CC} variables, and now we see that this advantage is retained after Step III as well.

Finally, one may wonder if there is any additional benefit in *combining* at Step III two or more of the variables considered in Table IX. We test this idea with the following exercise. Let us revisit Step III, again dropping the T_2 variable (27) from consideration, while for the definition

TABLE XI. The same as Table IX, but for a few representative methods from Table I which do not use mass information.

	Algorithm for Step I					
	$M_{T2}^{(b\ell)}$ and $m_{b\ell}$			$M_{2CC}^{(b\ell)}$ and $m_{b\ell}$		
	Correct	Wrong	Unresolved	Correct	Wrong	Unresolved
Step I: Quadrant counts	11,920	106	6,430	13,274	249	4,933
efficiency	$\varepsilon = 82.0\%$			$\varepsilon = 85.3\%$		
Remaining unresolved events	6,430			4,933		
m_t^{reco} with MAOS3$(b\ell;b\ell)$	3,527	2,903	-	2,980	1,953	-
cumulative efficiency	$\varepsilon = 83.7\%$			$\varepsilon = 88\%$		
m_t^{reco} with CMAOS3$(b\ell;b\ell)$	3,657	2,773	-	2,914	2,019	-
cumulative efficiency	$\varepsilon = 84.4\%$			$\varepsilon = 87.7\%$		
m_t^{reco} with $M_2A(b\ell)$	3,495	2,935	-	2,759	2,174	-
cumulative efficiency	$\varepsilon = 83.5\%$			$\varepsilon = 86.9\%$		
m_t^{reco} with $M_2A(\ell)$	3,719	2,711	-	2,699	2,234	-
cumulative efficiency	$\varepsilon = 84.7\%$			$\varepsilon = 88.6\%$		
m_W^{reco} with MAOS3$(b\ell;b\ell)$	3,877	2,553	-	2,783	2,150	-
cumulative efficiency	$\varepsilon = 85.6\%$			$\varepsilon = 87\%$		
m_W^{reco} with CMAOS3$(b\ell;b\ell)$	3,628	2,802	-	2,622	2,311	-
cumulative efficiency	$\varepsilon = 84.2\%$			$\varepsilon = 86.1\%$		
m_W^{reco} with $M_2A(b\ell)$	3,769	2,661	-	2,658	2,275	-
cumulative efficiency	$\varepsilon = 85\%$			$\varepsilon = 86.3\%$		
m_W^{reco} with $M_2A(\ell)$	3,448	2,982	-	2,529	2,404	-
cumulative efficiency	$\varepsilon = 83.3\%$			$\varepsilon = 85.6\%$		

of T_3 and T_4 let us choose the two best performing CMAOS variables from the right column of Table IX, namely m_t^{reco} with CMAOS1$(\ell; m_W)$ (87.9%) and m_W^{reco} with CMAOS1$(b\ell; m_t)$ (89.6%). In this modified scheme, we obtain a cumulative efficiency of $\varepsilon = 89.2\%$ with $N_C = 2$, 483 correctly identified, $N_W = 1$, 023 wrongly identified and $N_U = 1$, 427 unresolved events. Similarly, choosing the two best MAOS options in the middle column of Table IX, namely m_t^{reco} with MAOS1$(\ell; m_W)$ (87.4%) and m_W^{reco} with MAOS1$(b\ell; m_t)$ (88.8%), we find a final efficiency of $\varepsilon = 88.3\%$ (with $N_C = 3$, 493 correctly identified, $N_W = 1$, 176 wrongly identified and $N_U = 1$, 761 unresolved events). In both exercises, the final efficiency is slightly worse than what would be obtained with the single best variable alone, although the number of unresolved events decreased. These two exercises indicate that there exist nontrivial correlations between the different variables and an improvement of the efficiency is not guaranteed by simply merging or combining different methods. This is one of the reasons why we kept the results for the different methods separate in Table IX.

Up to this point, in Steps II and III we have used reconstruction methods which require the knowledge of a particle mass (m_t or m_W). However, when the method is being applied in studies of new physics, such information may not be immediately available. Therefore, it is prudent to consider modifications of Steps II and III, where one uses methods from Table I which do not rely on any mass information. To be specific, we focus on the four methods listed in the orange-shaded cells of Table I and show the corresponding results in Table XI, which is the direct analogue of Table IX. Once again, it turns out that Step II is unnecessary, albeit for a different reason—this time in all cases the solutions for the invisible momenta are found to be real and therefore invisible momentum reconstruction is always possible for both partitions. It also follows that there will be no unresolved events after Step III, since the relevant kinematic variables can always be computed and compared for the two partitions. The results in Table XI help identify the most promising variables for Step III—m_W^{reco} with MAOS3$(b\ell; b\ell)$ for the middle column ($\varepsilon = 85.6\%$) and m_t^{reco} with $M_2A(\ell)$ for the right column ($\varepsilon = 88.6\%$). In both cases, the use of a single variable at Step III leads to an improvement in the efficiency found after Step I of more than 3%.

In conclusion of this section, we summarize our main findings from the review of the method of Refs. [36,53].

1. The efficiency after Step I is increased if we define the quadrants of Fig. 6 in terms of $M_{2CC}^{(b\ell)}$ instead of $M_{T2}^{(b\ell)}$.

2. Step II does not lead to any appreciable effect after Step I, and can be safely omitted from the algorithm.

3. The use of the variable T_2 in Step III is counter-productive, thus T_2 can be safely dropped from consideration.

4. The use of a single optimal variable at Step III (as opposed to a combination of variables) is generally sufficient to produce the desired result.

V. A FEW IDEAS FOR FURTHER IMPROVEMENT

In the previous section, we considered the partitioning method as defined in Refs. [36,53] and found that with a few slight tweaks the efficiency (20) can reach over 89% (88%) with (without) mass information. In this section we shall consider a few more serious departures from the original algorithm, which can potentially further increase the efficiency. Some of the changes are simply quantitative (as in Sec. V A, where we increase the number of variables used at Step I), others are qualitative (as in Secs. V B and V C).

A. Generalizing the quadrant counts

Recall that the main idea at Step I was to use two kinematic variables, in this case $m_{b\ell}$ and $M_{T2}^{(b\ell)}$, which have clear kinematic endpoints for the case of the correct partition P_C. The resulting efficiency after Step I was 82%, and when we replaced $M_{T2}^{(b\ell)}$ with $M_{2CC}^{(b\ell)}$, the efficiency increased to 85.3%. But one should be able to do even better at Step I. The main point is that in the event topology of Fig. 1 there are not two, but *three* independent kinematic endpoints (they allow for a complete measurement of the mass spectrum [46,61]). Therefore, one can expect that the addition of a third variable at Step I, i.e., generalizing the plane of Fig. 6 to a three-dimensional parameter space divided into eight octants, would further improve the performance of Step I.
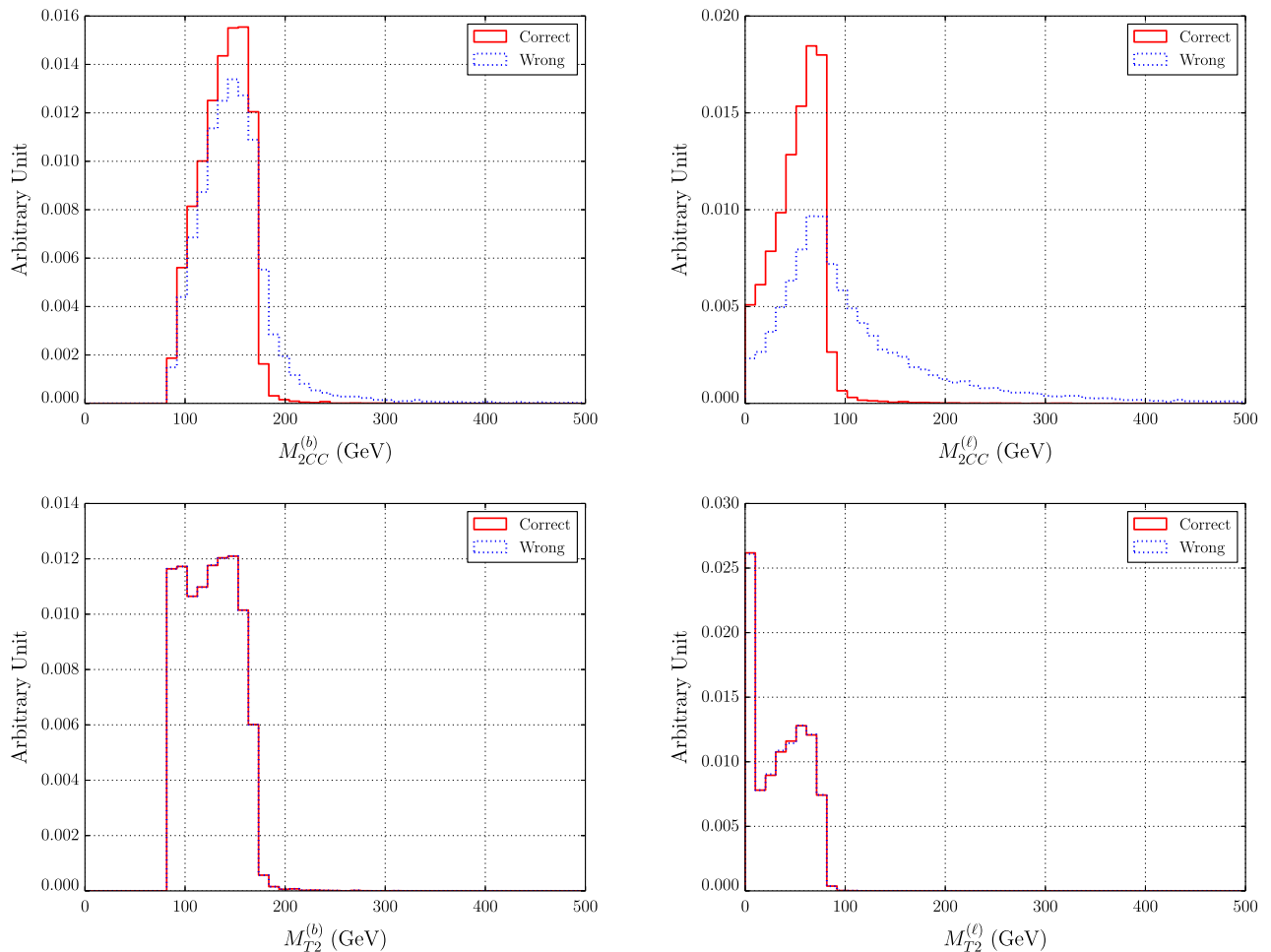

FIG. 9.   Distributions of M_{2CC} (top row) and M_{T2} (bottom row) for the case of subsystem (b) (left panels) or subsystem (ℓ) (right panels). The result for the correct (wrong) partition is shown in red (blue).

TABLE XII.   Octant counts utilizing the set of three variables (31), where rows (columns) are labelled by the sign signature $(\text{sign}(x), \text{sign}(y), \text{sign}(z))$ for the correct (wrong) partition.

$C\backslash W$	$(+,+,+)$	$(+,+,-)$	$(+,-,+)$	$(-,+,+)$	$(+,-,-)$	$(-,+,-)$	$(-,-,+)$	$(-,-,-)$
$(+,+,+)$	3,697	621	615	216	1,581	0	3,325	6,611
$(+,+,-)$	108	68	8	1	113	0	76	210
$(+,-,+)$	70	21	40	3	80	0	90	243
$(-,+,+)$	17	0	1	2	2	0	14	24
$(+,-,-)$	52	25	12	2	46	0	38	109
$(-,+,-)$	0	0	0	0	0	0	0	0
$(-,-,+)$	10	5	6	0	7	0	48	55
$(-,-,-)$	19	3	8	1	5	0	46	102

In order to test this idea, we need to pick a suitable third variable to go along with our original two. We focus on the M_{T2} and M_{2CC} variables in the remaining two subsystems, (b) and (ℓ), and show their distributions in Fig. 9. The plots in the bottom row indicate that the variables $M_{T2}^{(b)}$ and $M_{T2}^{(\ell)}$ are not suitable for our purpose since they do not depend on the chosen partition—the distributions for P_C (red solid lines) exactly coincide with the distributions for P_W (blue dotted lines). On the other hand, the distributions of $M_{2CC}^{(b)}$ (top left panel) and $M_{2CC}^{(\ell)}$ (top right panel) by construction depend on the partition via the mass shell constraint for the relative particle. The differences are more pronounced in the case of $M_{2CC}^{(\ell)}$, which we shall choose as our third variable to go along with the previous two, $m_{b\ell}$ and $M_{2CC}^{(b\ell)}$.

We can now generalize our previous discussion of the quadrant counts in Fig. 6 by populating our events in the three-dimensional space

$$(x, y, z) \equiv (m_{b\ell}^{\max} - \max_{j}\{m_{b\ell}^{(j)}\}, m_t - M_{2CC}^{(b\ell)}, m_W - M_{2CC}^{(\ell)}).$$
(31)

As before, we expect that for the correct partition P_C, the events will be populating predominantly the first octant, where $(\text{sign}(x), \text{sign}(y), \text{sign}(z)) = (+, +, +)$, while for the wrong partition P_W, the events will be more randomly distributed throughout the eight octants. These expectations

TABLE XIII.   Event counts summarizing the number of endpoint violations in Table XII. Unresolved events are in the diagonal entries, while events above (below) the diagonal are correctly (wrongly) resolved. The resulting final efficiency after Step I is 86.8%.

$C\backslash W$	0	1	2	3
0	3,697	1,452	4,906	6,611
1	195	144	375	477
2	62	50	139	164
3	19	12	51	102

are tested in Table XII, which generalizes the right table in Table IV by additionally incorporating the subsystem variable $M_{2CC}^{(\ell)}$. In Table XII, each of the eight octants of the parameter space (31) is labelled by its corresponding sign signature $(sign(x), sign(y), sign(z))$, and rows (columns) correspond to the correct (wrong) partition. Just like Table IV earlier, Table XII reveals that the endpoint violations are more likely to occur in the case of the wrong partition. We note that the entries in the $(-, +, -)$ row and column are identically zero—this is due to the fact that the values of $m_{b\ell}^{(j)}$ are direct input to the calculation of $M_{2CC}^{(b\ell)}$, so that once the $m_{b\ell}$ endpoint is violated in both decay chains ($j = 1$ and $j = 2$), it is very difficult to satisfy the endpoint of $M_{2CC}^{(b\ell)}$, unless the invisible momenta are rather soft (in the $b\ell$ rest frame). Note that under those circumstances the $M_{2CC}^{(\ell)}$ endpoint would be satisfied as well, which explains the nonzero entries in the $(-, +, +)$ row and column.

We are now in position to evaluate the effect of Step I in the presence of the additional variable—we simply compare the number of endpoint violations (0, 1, 2 or 3) for each partition P_k, and declare the winner P_C to be the case with fewer endpoint violations, as illustrated in Table XIII. The events for which both partitions give the same number of endpoint violations, remain unresolved—adding up the diagonal (unshaded) cells of Table XIII, we find $N_U = 4,082$. The events above (below) the diagonal cells are correctly (wrongly) resolved, giving $N_C = 13,985$ and $N_W = 389$, for a final efficiency of 86.8%.[16] This result should be contrasted with the 85.3% efficiency found in the right column of Table IX. Thus the benefit from adding a third variable to Step I can be quantified as an extra 1.5% in the efficiency.

B. Utilizing the variables $M_{2CW}^{(b\ell)}$ and $M_{2Ct}^{(\ell)}$

In this section we shall have in mind situations where full mass information is available, such as polarization studies

---

[16]We have checked that adding a fourth variable, $M_{2CC}^{(b)}$, and repeating the procedure in four dimensions, leads to a very marginal improvement: $N_U = 3,962$, $N_C = 14,076$ and $N_W = 418$, and efficiency of 87%.

TABLE XIV.   The same as Table XII, but using the set of variables (32).

C\W	(+,+,+)	(+,+,−)	(+,−,+)	(−,+,+)	(+,−,−)	(−,+,−)	(−,−,+)	(−,−,−)
(+,+,+)	2,388	500	353	0	2,526	0	187	8,662
(+,+,−)	69	41	8	0	124	0	6	352
(+,−,+)	157	26	65	0	156	0	23	809
(−,+,+)	0	0	0	0	0	0	0	0
(+,−,−)	174	70	15	0	485	0	6	879
(−,+,−)	0	0	0	0	0	0	0	0
(−,−,+)	11	1	5	0	3	0	2	38
(−,−,−)	21	2	6	0	34	0	1	251

in dilepton top events. Given the known values of m_t and m_W, the relevant question is whether they have been optimally utilized in the algorithm. With the MAOS method, this mass information is not used at all during the reconstruction of the *transverse* invisible components. One way to incorporate the mass information from the very beginning is to consider the additionally constrained variables $M_{2CW}^{(b\ell)}$ and $M_{2Ct}^{(\ell)}$ defined in (11) and (12), respectively [44]. We have already seen that those variables show the best performance in terms of reconstructing the neutrino momenta (see Figs. 2 and 3). This motivates us to perform Step I as in the previous section V A, but in terms of the alternative parameter space

$$(x, y, z) \equiv (m_{b\ell}^{max} - \max_j\{m_{b\ell}^{(j)}\}, m_t - M_{2CW}^{(b\ell)}, m_W - M_{2Ct}^{(\ell)})$$
(32)

instead of (31). The corresponding results are shown in Tables XIV and XV. We use the OPTIMASS package [67] to compute the values of $M_{2CW}^{(b\ell)}$ and $M_{2Ct}^{(\ell)}$. It should be noted that in certain cases OPTIMASS is unable to find a viable solution, since all constraints cannot be simultaneously satisfied. This can happen, e.g., when we consider the wrong partition of an event, or if some particles are produced off shell. For the purposes of tabulating the results in Tables XIV and XV, such cases are assigned a "minus" sign.

Table XV shows that when Step I is performed in terms of the alternative variables (32), the efficiency of Step I alone is as high as 88.1%. This is comparable to the results with several versions of the full algorithm (including Step

TABLE XV.   The same as Table XIII but based on the results from Table XIV. The final efficiency is 88.1%.

C\W	0	1	2	3
0	2,277	887	2,663	8,425
1	260	152	357	1,376
2	191	95	508	949
3	21	8	35	252

III) which were considered in the previous section. Thus we conclude that in cases where the masses of the intermediate particles are known, it is best to perform Step I in terms of the parameters (32) which use the variables $M_{2CW}^{(b\ell)}$ and $M_{2Ct}^{(\ell)}$.

C. Using reconstructed event kinematics: the $\sqrt{\hat{s}} - \cos\theta$ method

In this section, we shall use the fact that once we choose an ansatz for the invisible momenta via one of the methods from Table I, the full event kinematics is completely fixed as well. This means that when it comes to discriminating the unresolved events after Step I, we are not limited to only invariant mass variables, but we have the full set of kinematics tools at our disposal. In particular, we can study angular variables, as well as global inclusive variables, whose definition does not rely on partitioning the event.

An example of the latter type of variables is the total invariant mass in the event, $\sqrt{\hat{s}}$, where

$$\hat{s} \equiv \left(\sum_{j=1}^{2}(p_{a_j} + p_{b_j} + q_j)\right)^2.$$
(33)

It has been shown that a preselection cut on $\sqrt{\hat{s}}$ improves the efficiency at the cost of lowering the statistics [53]. This suggests that $\sqrt{\hat{s}}$ can potentially be a useful variable for categorizing the unresolved events after Step I. The idea is tested in the left panels of Fig. 10. The upper left panel shows $\sqrt{\hat{s}}$ distributions obtained with the $M_2A(b\ell)$ method from Table I, for the $N_U = 4,933$ unresolved events arising after Step I when it is done in terms of $M_{2CC}^{(b\ell)}$ and $m_{b\ell}$ (see the right columns in Tables IX and XI). The green dotted (blue dashed) line shows the case of the correct (wrong) partition. For reference, the solid red line gives the true $\sqrt{\hat{s}}$ distribution. As previously observed in Ref. [16], the reconstructed $\sqrt{\hat{s}}$ distribution peaks at threshold ($2m_t$). We also notice that the distribution for the wrong partition P_W is slightly harder, which suggests to investigate the ordered difference
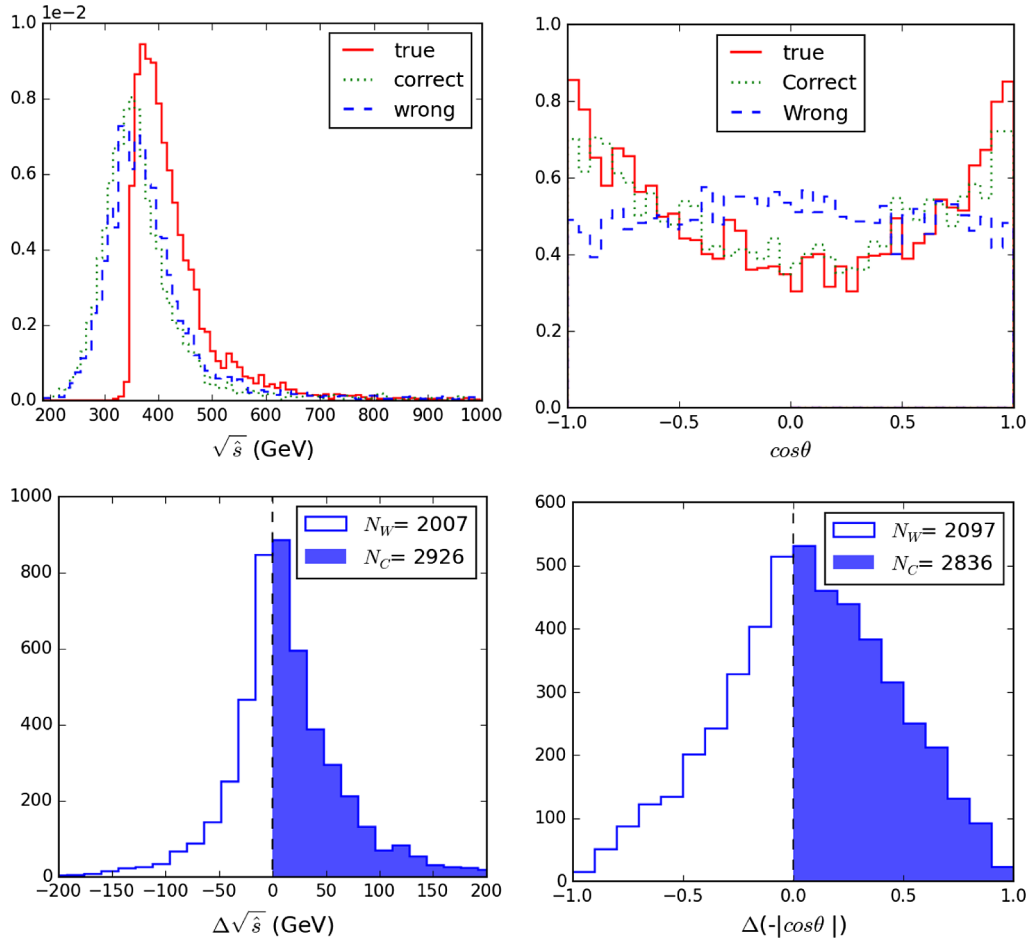
FIG. 10. Upper panels: unit-normalized distributions of the reconstructed variables $\sqrt{\hat{s}}$ (left) and $\cos\theta$ (right) for the unresolved events after Step I. The green dotted (blue dashed) lines correspond to results obtained with the correct (wrong) partition. The solid red line shows the MC truth distribution. Bottom plots: distributions of the ordered differences (34) (left panel) and (35) (right panel).

$$\Delta\sqrt{\hat{s}}(P_W, P_C) \equiv \sqrt{\hat{s}}(P_W) - \sqrt{\hat{s}}(P_C) \qquad (34)$$

in analogy to (30). The distribution of the variable (34) is shown in the lower left panel of Fig. 10. If we attempt to resolve events by applying the condition (24) to the variable $\sqrt{\hat{s}}$, we find $N_C = 2,926$ correctly resolved events (the shaded portion of the distribution in the lower left panel of Fig. 10) and $N_W = 2,007$ wrongly resolved events (the

TABLE XVI. Results from alternative methods for classifying the $N_U = 4,933$ unresolved events remaining after Step I when done in terms of $M_{2CC}^{(b\ell)}$ and $m_{b\ell}$. The two partitions are compared based on the resulting values of $\sqrt{\hat{s}}$, of $(-|\cos\theta|)$, or probabilistically based on the templates in Fig. 11.

method	N_C	N_W	N_U	ε
$\sqrt{\hat{s}}$	2926	2007	$\cdots$	87.8%
$-|\cos\theta|$	2836	2097	$\cdots$	87.3%
$\mathcal{P}(\sqrt{\hat{s}}, \cos\theta)$	3199	1720	14	89.2%

unshaded portion of the distribution). The overall efficiency is then increased from 85.3% after Step I to 87.8% (see Table XVI).

An alternative handle to sort the unresolved events is provided by the angular distribution of the parent particles at production. For concreteness, in the upper right panel of Fig. 10 we compare the distributions of the scattering angle θ of the top quarks in their center of mass frame, for the case of the correct partition (green dotted line), the wrong partition (blue dashed line) and the MC truth (solid red line). We notice that in reality, the top quarks are produced predominantly in the forward direction, due to the presence of t-channel and u-channel diagrams. When the momenta are reconstructed using the correct partition, this tendency is retained, while the distribution obtained with the wrong partition is mostly flat in $\cos\theta$. This motivates us to consider the corresponding ordered difference

$$\Delta(-|\cos\theta|)(P_W, P_C)$$
$$\equiv (-|\cos\theta|)(P_W) - (-|\cos\theta|)(P_C), \qquad (35)$$
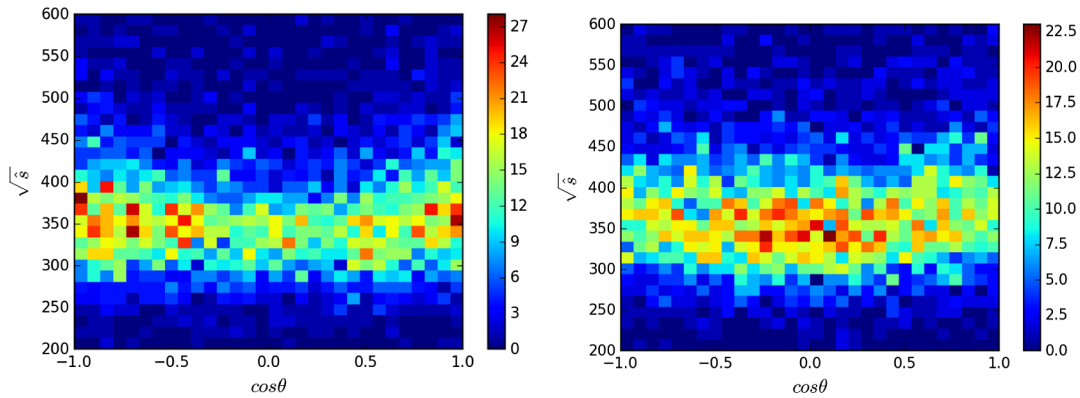
DEBNATH, KIM, KIM, KONG, and MATCHEV

FIG. 11. The two-dimensional templates $\mathcal{P}_C$ (left) and $\mathcal{P}_W$ (right) in the $(\cos\theta, \sqrt{\hat{s}})$ plane.

whose distribution is shown in the lower right panel of Fig. 10. As before, events with positive[17] values of the ordered difference (35) will be correctly resolved, and they represent the shaded portion of the distribution. As summarized in Table XVI, by applying the condition (24) to the $\cos\theta$ variable, we obtain $N_C = 2$, 836 ($N_W = 2$, 097) correctly (wrongly) resolved events and an overall efficiency of 87.3%.

Table XVI demonstrates that both variables $\cos\theta$ and $\sqrt{\hat{s}}$ are useful in categorizing the unresolved events, if applied separately. We now check whether they can be combined into a single method leading to an even higher efficiency. Since it is not possible to derive analytical expressions for the expected 2D distribution in $(\cos\theta, \sqrt{\hat{s}})$, we shall use a template method. Fig. 11 shows the relevant two-dimensional distributions using only unresolved events. In the left (right) plot the invisible momenta were reconstructed with the correct (wrong) partition. These two plots define two probability distributions, $\mathcal{P}_C$ and $\mathcal{P}_W$. Each of the two possible partitions P_k in an event comes with its own values of $\cos\theta$ and $\sqrt{\hat{s}}$, say $\cos\theta_k$ and $\sqrt{\hat{s}_k}$. Since we do not know whether P_1 corresponds to P_C or P_W, we try it both ways, and select

$$P_C = \begin{cases} P_1, & \text{if } \mathcal{P}_C(P_1)\mathcal{P}_W(P_2) > \mathcal{P}_C(P_2)\mathcal{P}_W(P_1); \\ P_2, & \text{if } \mathcal{P}_C(P_2)\mathcal{P}_W(P_1) > \mathcal{P}_C(P_1)\mathcal{P}_W(P_2). \end{cases}$$
(36)

As shown in Table XVI, the prescription (36) results in $N_C = 3$, 199 correctly resolved events and $N_W = 1$, 720 wrongly resolved events,[18] and the overall efficiency is

increased to 89.2%, which ranks among the best results we have found so far at the end of Step I.

VI. FINDING THE CORRECT PARTITION WITHOUT ANY MASS OR ENDPOINT INFORMATION

The potential improvements considered in the previous section relied on some prior knowledge about the masses of the particles involved in the decay chains. However, in new physics applications of our event topology from Fig. 1, such information may be difficult to get at first. This is why in this section we shall consider scenarios where no mass information is available, i.e., the masses of the particles A_i, B_i and C_i are *a priori* unknown, and furthermore, kinematic endpoint measurements are also unavailable or have very large uncertainties to be useful.

Let us now revisit the method under those assumptions. Steps I and II do require mass information (for defining the quadrants of Fig. 6 and for longitudinal momentum reconstruction, respectively) and therefore cannot be used. Similarly, two of the variables from Step III, namely ΔT_3 and ΔT_4, also need mass inputs for their calculation. For the moment, this leaves us with only ΔT_1 and ΔT_2 at our disposal. Since for the correct partition the values of T_1 and T_2 are in principle limited from above by a kinematic endpoint, we can still expect (23) to be mostly true. In fact, it is known that with the simple prescription (24) using ΔT_1 (ΔT_2) alone, the efficiency is 80% (79%) over all events [53]. As before, we can combine the two variables ΔT_1 and ΔT_2 and assign the correct partition P_C to be the one chosen by both variables. In order to estimate the resulting efficiency, in the first row of Table XVII we list the number of events with a given sign signature $\{\text{sign}[\Delta T_1(P_W, P_C)], \text{sign}[\Delta T_2(P_W, P_C)]\}$. The events with signature $(+, +)$ (green-shaded cells) will be correctly identified, the events with signature $(-, -)$ (red-shaded cells) will be wrongly identified, while the events with signatures $(+, -)$ or $(-, +)$ (unshaded cells) will remain unresolved at this point. The resulting efficiency of this combined $\Delta T_1 \oplus \Delta T_2$ method is 81.8%.

---

[17]This is why in the definition (35) we chose to consider the function $-|\cos\theta|$ instead of simply $|\cos\theta|$.

[18]The $N_U = 14$ unresolved events seen in Table XVI are due to our finite binning—for those events, the two points $(\cos\theta_k, \sqrt{\hat{s}_k})$, $k = 1, 2$, happened to fall within the same bin, which resulted in a tie. Since the templates of Fig. 11 are built from Monte Carlo, in principle one can use more statistics for their generation, and correspondingly smaller bin sizes, which will make such ties increasingly rare.

TABLE XVII.   Categorizing events by their sign signature for $(\Delta T_1, \Delta T_2)$ or $(\Delta T_1, \Delta T_5)$.

	$(+,+)$	$(+,-)$	$(-,+)$	$(-,-)$	efficiency
$(\text{sign}(\Delta T_1(P_W, P_C)), \text{sign}(\Delta T_2(P_W, P_C)))$	14,477	693	559	2,727	81.8%
$(\text{sign}(\Delta T_1(P_W, P_C)), \text{sign}(\Delta T_5(P_W, P_C)))$	14,677	493	1,003	2,283	83.6%

TABLE XVIII.   The same as Table XVII, but for the combined $\Delta T_1 \oplus \Delta T_5 \oplus \Delta T_6$ method. The resulting efficiency is 85.1%.

$(\text{sign}(\Delta T_1(P_W, P_C)), \text{sign}(\Delta T_5(P_W, P_C)), \text{sign}(\Delta T_6(P_W, P_C)))$							
$(+++)$	$(++-)$	$(+-+)$	$(-++)$	$(+--)$	$(-+-)$	$(--+)$	$(---)$
12,301	2,376	175	856	318	147	1,017	1,266

We emphasize that the $\Delta T_1 \oplus \Delta T_2$ method does not use any mass information: we simply compare the two possible values for $T_1(P_k)$ [as well as the two possible values for $T_2(P_k)$] for $k = 1$ and $k = 2$, and choose the larger (the smaller) to indicate the wrong (correct) partition. However, a potential problem with the method is that the variables T_1 and T_2 were found to be correlated [53]. This motivates us to look for an alternative set of variables. Since we saw previously that $M_{2CC}^{(b\ell)}$ is more efficient than $M_{T2}^{(b\ell)}$ (compare the middle and right panels in Fig. 5), we can try to replace T_2 with

$$T_5(P_i) \equiv M_{2CC}^{(b\ell)}(P_i). \tag{37}$$

The efficiency of the resulting $\Delta T_1 \oplus \Delta T_5$ method is 83.6%, as shown in the second row of Table XVII. One can go one step further and add a third variable to the mix, e.g., $M_{2CC}^{(\ell)}$, as was done in Sec. V A:

$$T_6(P_i) \equiv M_{2CC}^{(\ell)}(P_i). \tag{38}$$

The resulting combined method $\Delta T_1 \oplus \Delta T_5 \oplus \Delta T_6$ involves an odd number of variables, thus each event will be resolved based on the sign signature. This is illustrated in Table XVIII, which does not contain any unshaded cells. The corresponding efficiency of the method is 85.1%, which is a noticeable improvement over the results in Table XVII.

Until now, we have tested the efficiencies of the methods with a SM sample of dilepton $t\bar{t}$ events, i.e., the masses of the particles A_i, B_i and C_i were respectively the top mass m_t, the W-boson mass m_W, and the neutrino mass m_ν. One may wonder how sensitive the results are to the choice of a benchmark study point. This issue is investigated in Fig. 12, where we fix the mass of particle A to $m_A = 500$ GeV, and then freely vary the other two masses m_B and m_C. The left panel in Fig. 12 shows the efficiency of the $\Delta T_1 \oplus \Delta T_5 \oplus \Delta T_6$ method considered above. The efficiency varies noticeably throughout the mass parameter space, and seems to be correlated mostly with m_B and less with m_C. The highest efficiency is obtained in the region where the spectrum becomes relatively degenerate—in that case the visible decay products a_i and b_i are highly correlated with the direction of the parent particle A_i.

For completeness, in Fig. 12 we also show results for the standard hemisphere method [31–34] when applied to our event topology. In the hemisphere method, one clusters the visible particles into two groups trying to keep the invariant mass of each cluster to a minimum. It is not
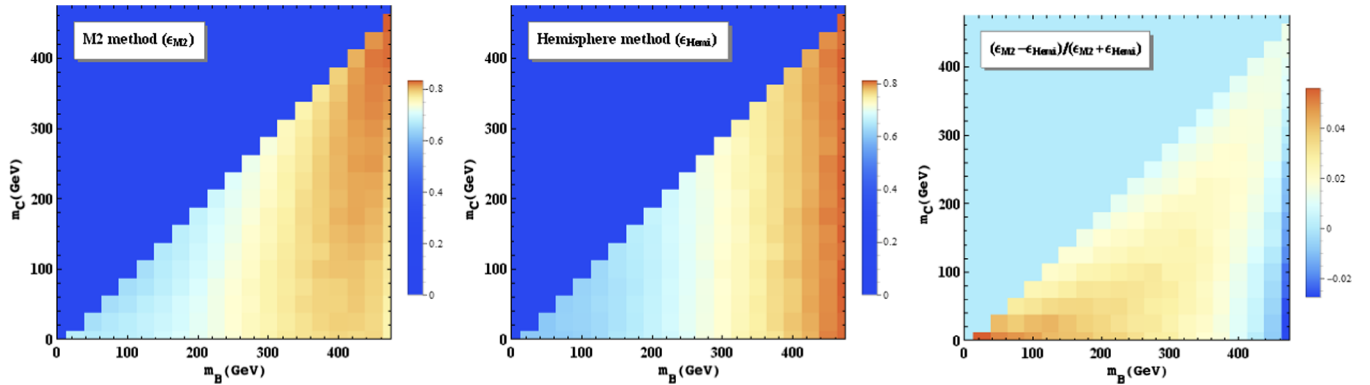

FIG. 12.   Efficiencies for choosing the correct partitioning for the $\Delta T_1 \oplus \Delta T_5 \oplus \Delta T_6$ method (left panel) and the hemisphere (i.e., ΔT_1) method (middle panel), as a function of the mass spectrum, for fixed $m_A = 500$ GeV and for $m_B > m_C$. The right panel compares the efficiencies of the two methods.

difficult to see that in our language this is nothing but the ΔT_1 method. The corresponding efficiency is shown in the middle panel of Fig. 12 and it exhibits the same qualitative behavior. The right panel of Fig. 12 compares the two methods by plotting the fractional difference of their efficiencies. We see that throughout most of the parameter space, the efficiency of the $\Delta T_1 \oplus \Delta T_5 \oplus \Delta T_6$ method is higher by 2–5%.

VII. SUMMARY AND OUTLOOK

The combinatorial problem is a very important issue in experimental particle physics. Identifying the correct event topology on an event by event basis is a key element of many analyses which attempt to measure particle properties such as spin, couplings, CP quantum numbers, etc. A successful method which can avoid combinatorial ambiguities, especially in jetty events, is bound to improve the sensitivity of new physics searches as well.

In this paper, we revisited some of the existing methods [36,53] for resolving the combinatorial ambiguity in the dilepton $t\bar{t}$ event topology of Fig. 1. To summarize our main findings:

1. The efficiency after Step I can be increased if a) the quadrants of Fig. 6 are defined in terms of $M_{2CC}^{(b\ell)}$ instead of $M_{T2}^{(b\ell)}$ and b) if the quadrants are generalized to "octants" as discussed in Sec. V A.

2. Step II does not lead to any appreciable effect after Step I, and can be safely omitted from the algorithm.

3. The use of the variable T_2 in Step III is counterproductive, and T_2 can also be dropped from consideration.

4. The use of a single optimal variable at Step III (as opposed to a combination of variables) is generally sufficient to produce the desired result.

5. The efficiency is also increased if the available mass information is incorporated as early as possible, e.g., by utilizing the variables $M_{2CW}^{(b\ell)}$ and $M_{2Ct}^{(\ell)}$, as discussed in Sec. V B.

6. We investigated further improvements of the algorithm, by invoking other types of variables, including a global inclusive variable like $\sqrt{\hat{s}}$ and an angular variable like $\cos\theta$, see Sec. V C.

7. In Sec. VI we discussed a more general approach which does not rely on any mass information.

One should keep in mind that the efficiency can always be further improved at the cost of statistics. For instance, a cut on $\sqrt{\hat{s}}_{\min}$ reduces the number of signal events, but the resulting efficiency can be increased beyond 90% [53].

Our results are directly applicable to any studies of final states containing $b\bar{b}W^+W^-$. Above all, they can be used for the study of SM dilepton $t\bar{t}$ events when performing precision measurements in the top quark sector. At the same time, in searches for new physics, where dilepton $t\bar{t}$ is the dominant background, our results should help in reducing the background and increasing the signal sensitivity. In addition, there are several interesting physics scenarios where a similar combinatorial problem plagues the signal itself:

(a) resonant di-Higgs production in the $b\bar{b}W^+W^-$ channel [71]; in this case, the dominant background is $t\bar{t} \rightarrow (bW^+)(\bar{b}W^-)$. The methods presented here can be applied to the $t\bar{t}$ background, but the signal may fail event reconstruction due to the inconsistent kinematics and/or event topology, and this could be used for background rejection.

(b) direct CP measurement of the Higgs-top coupling [72]; the observables proposed to measure the CP structure of the top Yukawa coupling typically assume reconstruction of the center-of-mass frame of the $t\bar{t}$ system with suppressed combinatorics. Our methods can therefore provide better reconstruction in the dilepton channel, allowing to study angular correlations through $\cos\theta^*$ [73] or $\Delta\phi_{\ell\ell}$ [72] with higher precision.

(c) constraining new resonant physics with top spin polarization information [74]; our M_2-based reconstruction can improve the results of Ref. [74], which made use of MAOS reconstruction.

(d) triple Higgs boson production [75,76], multi-boson production processes such as $W^\pm W^\mp H$ or $W^\pm W^\mp HH$ [77], studies of anomalous triple and quartic gauge coupling such as $W^+W^-\gamma$, W^+W^-Z, $\gamma\gamma W^+W^-$ and $\gamma Z W^+W^-$ [78–80]; all these are natural extensions of the $hh \rightarrow (b\bar{b})(W^+W^-)$ process mentioned above.

We emphasize that our methods may be generalized to the case of more complicated decays of pair-produced heavy states, as long as the final state contains two missing particles (one per decay side).

Looking ahead, there are several directions in which the study presented here can be evolved.

1. Following the previous literature, in this initial investigation we considered a relatively simple situation, where there were only two possible alternatives, and we had to pick one of them. As we increase the number of indistinguishable objects in the final state, things get much more complicated. We intend to tackle this more difficult problem in the very near future.

2. As the number of jets in the signature is increased, it becomes important to cross-check the parton-level results with more detailed simulations including detector effects, initial and final state radiation, etc.

3. The kinematic variables which we used here were designed for event topologies with two missing particles. It would be interesting to generalize our analysis to event topologies with more than two missing particles, where one would have to use a different set of M_2 variables suitably adapted for that case.

[1] S. Chatrchyan *et al.* (CMS Collaboration), J. Instrum. **6**, P09001 (2011).
[2] S. Chang and A. de Gouvea, Phys. Rev. D **80**, 015008 (2009).
[3] K. Agashe, D. Kim, M. Toharia, and D. G. E. Walker, Phys. Rev. D **82**, 015007 (2010).
[4] K. Agashe, D. Kim, D. G. E. Walker, and L. Zhu, Phys. Rev. D **84**, 055020 (2011).
[5] G. F. Giudice, B. Gripaios, and R. Mahbubani, Phys. Rev. D **85**, 075019 (2012).
[6] W. S. Cho, D. Kim, K. T. Matchev, and M. Park, Phys. Rev. Lett. **112**, 211801 (2014).
[7] K. Agashe, R. Franceschini, D. Kim, and K. Wardlow, Phys. Dark Universe **2**, 72 (2013).
[8] A. J. Barr, T. J. Khoo, P. Konar, K. Kong, C. G. Lester, K. T. Matchev, and M. Park, Phys. Rev. D **84**, 095031 (2011).
[9] T. Plehn, D. Rainwater, and P. Z. Skands, Phys. Lett. B **645**, 217 (2007).
[10] J. Alwall, S. de Visscher, and F. Maltoni, J. High Energy Phys. 02 (2009) 017.
[11] A. Papaefstathiou and B. Webber, J. High Energy Phys. 06 (2009) 069.
[12] P. Jackson, C. Rogan, and M. Santoni, Phys. Rev. D **95**, 035031 (2017).
[13] A. J. Barr and C. G. Lester, J. Phys. G **37**, 123001 (2010).
[14] I. Hinchliffe, F. E. Paige, M. D. Shapiro, J. Soderqvist, and W. Yao, Phys. Rev. D **55**, 5520 (1997).
[15] D. R. Tovey, Phys. Lett. B **498**, 1 (2001).
[16] P. Konar, K. Kong, and K. T. Matchev, J. High Energy Phys. 03 (2009) 085.
[17] J. Hubisz, J. Lykken, M. Pierini, and M. Spiropulu, Phys. Rev. D **78**, 075008 (2008).
[18] C. G. Lester and D. J. Summers, Phys. Lett. B **463**, 99 (1999).
[19] B. C. Allanach, C. G. Lester, M. A. Parker, and B. R. Webber, J. High Energy Phys. 09 (2000) 004.
[20] C. Lester and A. Barr, J. High Energy Phys. 12 (2007) 102.
[21] J. Alwall, K. Hiramatsu, M. M. Nojiri, and Y. Shimizu, Phys. Rev. Lett. **103**, 151802 (2009).
[22] Y. Bai and H. C. Cheng, J. High Energy Phys. 06 (2011) 021.
[23] D. Wiesler, Report No. DESY-THESIS-2012-048.
[24] P. S. B. Dev, D. Kim, and R. N. Mohapatra, J. High Energy Phys. 01 (2016) 118.
[25] D. Kim, K. T. Matchev, and M. Park, J. High Energy Phys. 02 (2016) 129.
[26] M. D. Klimek, J. High Energy Phys. 12 (2016) 132.
[27] D. Debnath, J. S. Gainer, C. Kilic, D. Kim, K. T. Matchev, and Y. P. Yang, J. High Energy Phys. 06 (2017) 092.
[28] J. H. Shim and H. S. Lee, Phys. Rev. D **89**, 114023 (2014).
[29] D. Krohn, L. Randall, and L. T. Wang, arXiv:1101.0810.
[30] D. Kim and K. Kong, Phys. Lett. B **751**, 512 (2015).
[31] G. L. Bayatian *et al.* (CMS Collaboration), J. Phys. G **34**, 995 (2007).
[32] S. Matsumoto, M. M. Nojiri, and D. Nomura, Phys. Rev. D **75**, 055006 (2007).
[33] W. S. Cho, K. Choi, Y. G. Kim, and C. B. Park, J. High Energy Phys. 02 (2008) 035.
[34] M. M. Nojiri, Y. Shimizu, S. Okada, and K. Kawagoe, J. High Energy Phys. 06 (2008) 035.
[35] A. Rajaraman and F. Yu, Phys. Lett. B **700**, 126 (2011).
[36] P. Baringer, K. Kong, M. McCaskey, and D. Noonan, J. High Energy Phys. 10 (2011) 101.
[37] M. M. Nojiri, K. Sakurai, Y. Shimizu, and M. Takeuchi, J. High Energy Phys. 10 (2008) 100.
[38] P. Jackson and C. Rogan, arXiv:1705.10733.
[39] M. M. Nojiri, G. Polesello, and D. R. Tovey, arXiv:hep-ph/0312317.
[40] K. Kawagoe, M. M. Nojiri, and G. Polesello, Phys. Rev. D **71**, 035008 (2005).
[41] H. C. Cheng, J. F. Gunion, Z. Han, G. Marandella, and B. McElrath, J. High Energy Phys. 12 (2007) 076.
[42] H. C. Cheng, D. Engelhardt, J. F. Gunion, Z. Han, and B. McElrath, Phys. Rev. Lett. **100**, 252001 (2008).
[43] H. C. Cheng, J. F. Gunion, Z. Han, and B. McElrath, Phys. Rev. D **80**, 035020 (2009).
[44] D. Kim, K. T. Matchev, F. Moortgat, and L. Pape, J. High Energy Phys. 08 (2017) 102.
[45] A. Barr, C. Lester, and P. Stephens, J. Phys. G **29**, 2343 (2003).
[46] M. Burns, K. Kong, K. T. Matchev, and M. Park, J. High Energy Phys. 03 (2009) 143.
[47] A. J. Barr, B. Gripaios, and C. G. Lester, J. High Energy Phys. 11 (2009) 096.
[48] P. Konar, K. Kong, K. T. Matchev, and M. Park, J. High Energy Phys. 04 (2010) 086.
[49] P. Konar, K. Kong, K. T. Matchev, and M. Park, Phys. Rev. Lett. **105**, 051802 (2010).
[50] W. S. Cho, K. Choi, Y. G. Kim, and C. B. Park, Phys. Rev. D **79**, 031701 (2009).
[51] C. B. Park, Phys. Rev. D **84**, 096001 (2011).
[52] D. Guadagnoli and C. B. Park, J. High Energy Phys. 01 (2014) 030.
[53] K. Choi, D. Guadagnoli, and C. B. Park, J. High Energy Phys. 11 (2011) 117.

[54] R. Mahbubani, K. T. Matchev, and M. Park, J. High Energy Phys. 03 (2013) 134.

[55] W. S. Cho, J. S. Gainer, D. Kim, K. T. Matchev, F. Moortgat, L. Pape, and M. Park, J. High Energy Phys. 08 (2014) 070.

[56] G. G. Ross and M. Serna, Phys. Lett. B **665**, 212 (2008).

[57] S. Chatrchyan et al. (CMS Collaboration), Eur. Phys. J. C **73**, 2494 (2013).

[58] ATLAS Collaboration, Report No. ATLAS-CONF-2012-082.

[59] T. H. N. Phan, Report No. CERN-THESIS-2013-173, BONN-IB-2013-02.

[60] A. M. Sirunyan et al. (CMS Collaboration), Phys. Rev. D **96**, 032002 (2017).

[61] W. S. Cho, J. S. Gainer, D. Kim, K. T. Matchev, F. Moortgat, L. Pape, and M. Park, J. High Energy Phys. 05 (2015) 040.

[62] J. Reuter and D. Wiesler, Phys. Rev. D **84**, 015012 (2011).

[63] K. Choi, S. Choi, J. S. Lee, and C. B. Park, Phys. Rev. D **80**, 073010 (2009).

[64] W. S. Cho, K. Choi, Y. G. Kim, and C. B. Park, Nucl. Phys. B **200–202**, 103 (2010).

[65] K. Choi, J. S. Lee, and C. B. Park, Phys. Rev. D **82**, 113017 (2010).

[66] J. Alwall, R. Frederix, S. Frixione, V. Hirschi, F. Maltoni, O. Mattelaer, H.-S. Shao, T. Stelzer, P. Torrielli, and M. Zaro, J. High Energy Phys. 07 (2014) 079.

[67] W. S. Cho, J. S. Gainer, D. Kim, S. H. Lim, K. T. Matchev, F. Moortgat, L. Pape, and M. Park, J. High Energy Phys. 01 (2016) 026.

[68] D. R. Tovey, J. High Energy Phys. 04 (2008) 034.

[69] K. T. Matchev and M. Park, Phys. Rev. Lett. **107**, 061801 (2011).

[70] W. S. Cho, J. E. Kim, and J. H. Kim, Phys. Rev. D **81**, 095010 (2010).

[71] T. Huang, J. M. No, L. Perni, M. Ramsey-Musolf, A. Safonov, M. Spannowsky, and P. Winslow, Phys. Rev. D **96**, 035007 (2017).

[72] M. R. Buckley and D. Goncalves, Phys. Rev. Lett. **116**, 091801 (2016).

[73] ATLAS Collaboration, Report No. ATLAS-CONF-2016-100.

[74] C. Englert, J. Ferrando, and K. Nordstrm, Eur. Phys. J. C **77**, 407 (2017).

[75] A. Papaefstathiou and K. Sakurai, J. High Energy Phys. 02 006 (2016).

[76] B. Fuks, J. H. Kim, and S. J. Lee, Phys. Lett. B **771**, 354 (2017).

[77] C. Englert, Q. Li, M. Spannowsky, M. Wang, and L. Wang, Int. J. Mod. Phys. A **32**, 1750106 (2017).

[78] J. M. Kunkle, in *DPF 2015 Meeting of the American Physical Society Division of Particles and Fields, Ann Arbor, Michigan*, 2015, http://inspirehep.net/search?ln=en&ln=en&p=find+t+2015+and+t+proceedings+and+t+DPF&of=hb&action_search=Search&sf=earliestdate&so=d&rm=&rg=50&sc=0.

[79] M. Aaboud et al. (ATLAS Collaboration), Phys. Rev. D **96**, 012007 (2017).

[80] V. Khachatryan et al. (CMS Collaboration), Phys. Rev. Lett. **114**, 051801 (2015).